Impact of ultrasonic welding on multi-layered Al-Cu joint for electric vehicle battery applications: A layer-wise microstructural analysis

Sisir Dhara[a], Abhishek Das[a]*

[a] *WMG, University of Warwick, Coventry, CV4 7AL, UK*
**Corresponding author: A.Das.1@warwick.ac.uk*

Abstract

Multi-layered aluminium (Al) tabs to copper (Cu) busbar joints are increasingly being used for electric vehicle (EV) battery applications. Being a solid-state joining process, ultrasonic welding (USW) offers several benefits including less intermetallic or no porosity formation and larger weld area compared to fusion type welding, especially for highly conductive /reflective multi-layered dissimilar materials welding. In spite of being a suitable joining process, the impact of ultrasonic process parameters needs in-depth analysis for multi-layered stack-up where the process parameters play a pivotal role to join the layers of weldments. In this study, three layers of 0.3 mm Al tabs were welded to 1.0 mm single Cu busbar for the investigations of multi-layered Al-Cu dissimilar joints. Joint macro and microstructures, welding mechanism, layer-wise micro-hardness and grain formation were studied to understand the flow of material, the formation of grains and mixing of the Al and Cu for under-weld, good-weld and over-weld categories. The effects of amplitude of ultrasonic vibration, welding pressure and welding time were investigated to produce the satisfactory tab-to-busbar connection. The layer-wise microstructural study revealed the welding mechanism, propagation of micro-bonds and flow of material. The micro-hardness study unveiled different weld zones indicating the area of material mixing and the affected region whereas the crystallographic orientation maps disclosed the grain formation and recrystallization after the welding. The results showed that interfacial material mixing, wave-like material flow and interfacial micro-bonds formation were the prominent reasons for the satisfactory ultrasonic weld.

Keywords: Ultrasonic welding; multi-layered dissimilar joints; weld microstructure; micro-hardness distribution; grain formation; fractography.

1 Introduction

Recent uptake of electric vehicles and advancement in automotive technology urge improved techniques to meet the environmental challenges and market demand. Electric vehicles, hybrid or plug-in hybrid electric vehicles are increasingly being used for the reduction of emission of greenhouse gases and meeting the national and international legislation on emission target [1]. The battery pack used within these vehicles are composed of a large number of battery cells, which are electrically connected and structurally held [2]. For example, in case of pouch cell based battery pack, cell tabs are to be connected with the busbar for making the successful electrical connection. However, the making of those connections is not trivial as multi-layered stack-up, highly reflective and conductive materials are to be joined. Therefore, there is a need for suitable joining techniques to address the need for manufacturing the battery pack. For example, multiple tabs protruded from the battery cell terminals are welded with the busbar within the battery pack of the electric vehicle [3]. Joint strength and electrical conductivity of tab to busbar joint are extremely important criteria for a successful connection [4]. The electrical conductivity through the weldments should be high enough so that the energy loss would be minimum possible [3], [5]. In addition, the joint strength should be sufficient to withstand all the impact and vibrational forces [3], [6].

To address the aforesaid challenges and requirements, a number of joining techniques are being investigated for battery pack manufacturing [7], [8] including conventional fusion welding and solid-state welding. In general, conventional fusion welding is associated with many problems ranging from brittle intermetallic formation to distortion in weldments [6], [9]. In addition, conventional fusion welding may not be suitable for highly conductive and reflective metals when large welding nugget is expected. As a solution to these problems, solid-state welding becomes popular due to the elimination of the metallurgical defects such as the formation of intermetallic compounds (IMC), brittle phases and porosities in the fused zone liquid phase reactions [10], [11], [12]. Two prominent solid-state welding processes are friction stir welding (FSW) and ultrasonic welding (USW). However, the application of FSW is restricted due to the formation of brittle intermetallic phases in the weldments and incapability to joint thin sheets effectively [13], [14], [15]. In contrast, USW is one of the promising techniques to join these multi-layered stack-ups for automotive battery manufacturing [6], [16]. As a solid-state welding process, USW avoids melting of the materials and joins them based on diffusion and adhesion of the softened metals due to interfacial friction [3], [17]. USW seems advantageous in this case, as it provides necessary joint strength and it offers low or no brittle intermetallic layers along the weld line, which ensures less electrical resistance [6], [18], [19]. Hence, this process is suitable for highly conductive and reflective soft metals such as aluminium, copper, brass, silver and gold [20]. Therefore, USW emerges as an appropriate technique for thin sheets welding applicable to various electric vehicle battery, electrical and electronics industries.

The working principle of USW system can be explained in a few steps. A piezoelectric transducer converts the electrical energy to the shear vibration of the sonotrode, which helps the samples to joint together with the help of clamping force [21], [22]. At first, the surface oxide layers are removed from the sample interface [23] and material gets softened due to temperature rise at the sample interface. This ultrasonic vibration creates a diffusion of metals and subsequently adhesion [20]. Several bonding mechanisms were reported in the literature including interfacial diffusion, adhesion due to plastic deformation, local heating and mechanical interlocking [24]. However, the exact bonding mechanism varies from metal to metal due to the change in material properties and depends on the stack-up combination.

Various researchers had investigated the welding mechanism, optimal parametric conditions, joint strength and reliability of ultrasonic welds. USW of diverse combinations of metal or non-metal sheets such as Al-Cu, Al-steel, metal-ceramic and metal-glass was reported in the literature [25], [26]. Bakavos and Prangnell [21] studied the mechanism of Al-Al and reported that interfacial convolutes, swirls, ripples and micro-bonding were the mechanisms behind the weld. Chen et al. [27] studied the interfacial heat-affected zone (HAZ) along the weld line and explained that due to increase of interfacial temperature to a sufficiently high level (400° C), the softening became very swift and recovery was at a much faster rate than parent metal due to natural ageing. There are few measures adapted by researchers to evaluate weld quality. For example, several researchers tried to quantify bond quality in USW. Linear weld density was presented to quantify weld quality by Kong et al. [28]. The ratio of an actual bonded line along the weld interface to the entire weld along the weld interface was termed as linear weld density and it was used as a quantitative weld quality criterion for ultrasonic welds. Hu et al. [29] proposed peel test to analyse bond quality. The higher strength, a material offered during peeling it off from the weld, represented the higher bond quality. Hetrick et al. [30] assessed various microstructural phenomenon (i.e. various distances within the weld zone including peak and valley heights from the weld line) to describe the bonding of USW. A comprehensive evaluation was conducted by Lee et al. [6], where they studied bond density, post-weld thickness, thermomechanically affected zone (TMAZ) to characterize weld quality based on a single-layered joint of 0.4 mm pure Cu sheet with 1 mm Ni plated Cu sheet. It was found that microhardness played an important role to explain the work hardening and thermal softening during USM and segregated the TMAZ from the base metal (BM) [6], [17]. For example, Macwan et al. [31] studied layer-wise micro-hardness values of multi-layered Al-Mg joints and correlated them with the weld strength observed from lap shear tests. Hence, the measurement of micro-hardness is an integral part to evaluate weld quality. Furthermore, Prangnell et al. [19] and Haddadi et al. [18] observed high-resolution electron back scattered diffraction (EBSD) Euler contrast maps at the weld interface of Al-Steel joint and investigated the dynamic recrystallization phenomena by analysing the grain size at the weld interface. Thus, EBSD study would reveal the grain formation and recrystallization phenomena of grains for different weld conditions. However, grain formation and recrystallization for multi-layered ultrasonic weld are not reported in the literature, and subsequently, their effects on the ultrasonic weld quality need to be addressed.

Few studies were conducted considering Al-Cu dissimilar material combination. For example, single layer based dissimilar Al-Cu joint was studied by Satpathy and Sahoo [16], Zhao et al. [11] and Balasundaram et al. [32] where they explored welding mechanism and micro-hardness distribution. In addition, Wu et al. [3] extended their study for multi-layered Al-Cu joint and they investigated the weld formation mechanism and failure modes using the lap shear test. Multi-layered dissimilar Al-Cu welding is essential for electric vehicle battery applications; however, extensive investigations are not performed yet. Therefore, this study focussed on in-depth weld mechanism study, layer-wise micro-hardness analysis and grain formation study for multi-layered dissimilar Al-Cu joint.

In this study, three layers of 0.3 mm Al sheet (i.e. representative of battery tabs) were welded to the single layer of 1.0 mm Cu sheet (i.e. representative of battery busbar) using USW and the impact of ultrasonic welding parameters on this multi-layered dissimilar materials were investigated. The welding mechanism of this multi-layered joint was investigated by observing material flow, interfacial material mixing and micro-bond formation with the help of optical microscopy. To reveal the various weld zones related to work hardening and thermal softening phenomena, the layer-wise micro-hardness measurement was carried out. Furthermore, this helped to segregate the TMAZ from the BM. Moreover, grain formation at the weld interface as well as under the sonotrode tip was investigated by observing grain size and dynamic recrystallization using high-resolution EBSD Euler maps. Grain formation analysis helped to understand the layer-wise welding mechanism better in a multi-layered USW weldment.

2 Materials and methods

Aluminium (Al) sheet of 0.3 mm was chosen as tab material and 1.0 mm copper (Cu) sheet was selected as busbar. Chemical composition of both the metals are detailed in Table 1. Samples with 100 mm length and 25 mm width were cut from the sheet metals for the preparation of welding specimens. Two different types of welding specimens were prepared, such as lap shear (refer to Fig. 1c) and T-peel (refer to Fig. 1d) configurations. During the preparation of both the configurations, a single layer of Cu sample was kept at the bottom whereas three layers of Al samples were kept on top of the Cu layer. For both the configuration, 25 mm overlap of Al and Cu samples was ensured. The welding of the specimens was carried out by using Telsonic MPX ultrasonic welder. The maximum power and maximum force of this welder were 6.5 kW and 5 kN respectively. Peak to peak maximum amplitude of ultrasonic vibration was 60µm. The trigger mode time (time for converting traversing pressure to welding pressure) was kept at 0.2 s. The sonotrode covered a weld area of 10×5 mm^2. The detailed diagram of the welding set-up is depicted in Fig. 1a-b. Fig. 1e represents the schematic of the weld geometry with defined layers and interfaces. In this study, three Al layers are denoted as: (i) Al layer 1 or Al_{top} layer (i.e. the top Al sheet), (ii) Al layer 2 or Al_{middle} layer (i.e. the middle Al sheet) and (iii) Al later 3 or Al_{bottom} layer (i.e. the bottom Al sheet). Similarly for the interfaces, the notations are used as: (i) Al-Al interface 1 (i.e. interface in between Al_{top} layer and Al_{middle} layer), (ii) Al-Al interface 2 (i.e. interface in between Al_{middle} layer and Al_{bottom} layer) and (iii) Al-Cu interface (i.e. interface in between Al_{bottom} layer and Cu sheet). These notations are used throughout the entire paper.

Table 1: Chemical composition of metals investigated in this study.

Material	Grade	Chemical composition (wt%)
Aluminium (Al)	AW1050A-H18; BS EN546	Si < 0.25, Fe < 0.40, Cu < 0.05, Mn < 0.05, Mg < 0.05, Zn < 0.07, Ti < 0.05, Al-balance 99.50
Copper (Cu)	CW004A-H065; BS EN1652 (C101HH; BS 2870)	Cu > 99.99, O < 0.0005, other-balance

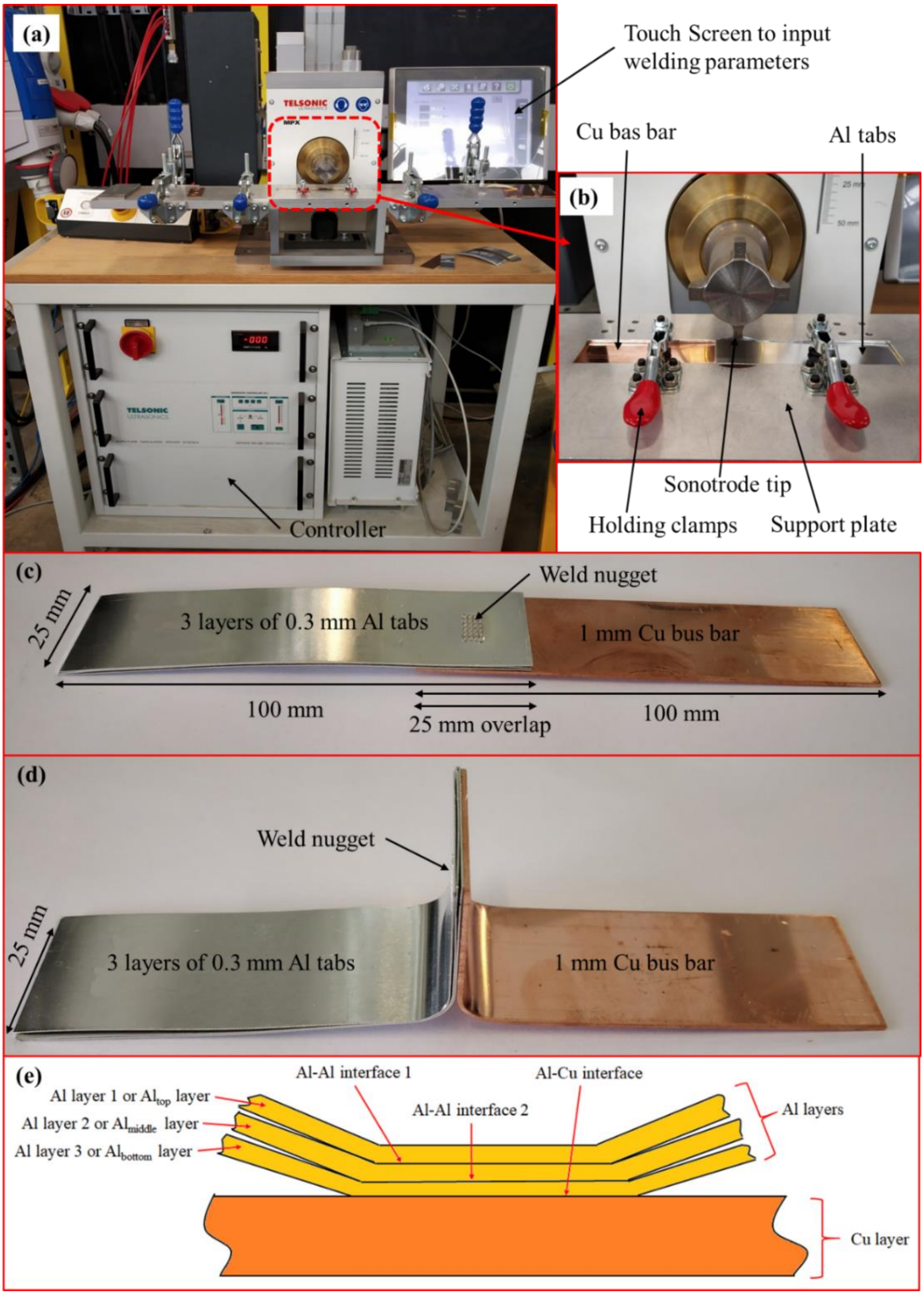

Fig. 1: USW set-up: (a) USW machine, (b) welding head with sonotrode and clamps for holding the work specimens, (c) lap shear joint configuration, (d) T-peel joint configuration and (e) schematic representation of weld joint.

During performing ultrasonic welding, three input parameters namely amplitude of ultrasonic vibration (denoted as amplitude), welding pressure (denoted as pressure) and welding time (denoted as time) were varied one at a time while other input parameters were kept constant.

The input parameters with the various levels are shown in Table 2. The values of constant input parameters throughout the entire study were: frequency of ultrasonic vibration was 20 kHz, peak to peak amplitude of ultrasonic vibration was 60 μm, holding time after welding was 0.3 s and joining area was 10 × 5 mm^2. Based on the joint strength and failure mode during lap shear and T-peel tests, the welded specimens were categorised into three different groups namely under-weld, good-weld and over-weld. Lap shear and T-peel tests were conducted to evaluate joint strength by applying 10 kN load in an Instron 5800 machine. Crosshead speeds were kept at 2 mm/min and 10 mm/min for lap shear and T-peel tests respectively. The detailed procedure of the selection of weld category was described in the literature [33].

Table 2: Input parameter variations adopted in this study.

Input parameter variations with corresponding weld energy					Constant parameters during each variation
Input parameters	Variation levels				
Amplitude, *a* (μm)	40 μm	45 μm	50 μm	55 μm	Pressure: 1 bar Time: 0.60 sec
Corresponding average weld energy	310 J	427 J	615 J	790 J	
Pressure, *p* (bar)	1 bar	2 bar	3 bar	4 bar	Amplitude: 50 μm Time: 0.60 sec
Corresponding average weld energy	615 J	655 J	734 J	741 J	
Time, *t* (second)	0.15 sec	0.30 sec	0.45 sec	0.60 sec	Amplitude: 50 μm Pressure: 1 bar
Corresponding average weld energy	111 J	269 J	427 J	615 J	

To investigate the welding mechanism, weld zones and grain formation for three different weld categories, namely under-weld, good-weld and over-weld, several microstructural analyses were conducted. The welded samples of these three weld categories were cut along the cross-section and were cold mounted; and subsequently polished using SiC abrasive paper, diamond suspension solutions and colloidal silica solution. Microstructural analysis was performed by observing weld microstructures in Nikon Eclipse LV150N optical microscope (OM) and ZEISS SIGMA field emission scanning electron microscope (FE-SEM) equipped with electron backscattered diffraction (EBSD) systems. EBSD scanning was done with 0.5 μm step size. Vickers micro-hardness of the weld samples was measure by using fully automatic Buehler's

Wilson VH1202 micro-hardness testing machine by applying 50 gm force (i.e. 0.49 N) for 10 sec dwell time. Fractography was conducted by observing fracture surface, obtained during lap shear and T-peel tests, in the ZEISS SIGMA FE-SEM.

3 Results

3.1 Lap shear and T-peel strengths

Lap shear and T-peel are the two important tests to check the weld strength. A good-weld always imparts a satisfactory strength during the lap shear and T-peel tests. In the previous study by Das et al. [33], lap shear and T-peel tests of USW welded samples were carried out and subsequently, all the welded samples were classified into three weld categories (i.e. under-weld, good-weld and over-weld) according to the load-displacement features and failure modes obtained from lap shear and T-peel tests. The same approach was adapted in this study to classify the welds into the three weld categories. Understanding the effect of input parameters on weld strength is an important aspect to visualize how the input parameters play an important role in weld mechanism. To realise the main effects of input parameters, three main input parameters were varied which were amplitude, pressure and time. This was obtained by varying one parameter at a time while keeping the other parameters at a constant value. The details of the input parameter variations are presented in Table 2.

The effects of input parameters i.e. amplitude, pressure and time on maximum load obtained from the lap shear and T-peel tests are depicted in Fig. 2. The effect of amplitude on the maximum load during lap shear and T-peel tests is shown in Fig. 2a. Amplitude variation changed the maximum load at lap shear test within the limit of 371 N (i.e. 1534 N lap shear load was obtained at 40 μm amplitude and increased to 1905 N at 45 μm and thereafter gradually decreased to 1770 N at 55 μm amplitude) whereas it changed the T-peel maximum load around 500 N (i.e. 113 N T-peel load was obtained at 40 μm amplitude and gradually increased to 613 N at 55 μm). In contrast, increasing pressure had a decreasing effect on both maximum lap shear and T-peel loads. For example, maximum lap shear and T-peel loads were decreased by around 632 N and 302 N respectively when the pressure was increased from 1 bar to 4 bar as indicated in Fig. 2b. Fig. 2c shows that the time variation increased the maximum load obtained from the lap shear test by 676 N while the maximum load obtained from T-peel test was increased by 344 N due to incremental increase in the welding time from 0.15 sec to 0.60 sec. It was prominent that the maximum load during lap shear tests reduced gradually with the increase of pressure, whereas higher time helped to improve maximum load during lap shear tests. Amplitude variation did not play a major role as it improved the maximum load during lap shear tests by a small amount. On the other hand, amplitude variation played a significant role in improving the maximum load during T-peel tests. Both the higher amplitude and higher time increased the maximum load during T-peel tests, however, a high welding pressure reduced the maximum load obtained from T-peel tests. Hence, pressure and time were the two main parameters to improve the lap shear strength of a joint while amplitude and time were the most critical parameter for improving T-peel strength. Overall, time is the most critical parameter for improving both lap shear and T-peel joint strengths followed by pressure and amplitude.

Variation in input parameters played a significant role in deriving the weld categories from lap shear and T-peel tests. The methodology to derive the weld categories from lap shear and T-peel tests results were described in the literature [33]. The effect of input parameter variations on weld category is summarized in Table 3. Amplitude variation helped the weld category to be elevated from under-weld to good-weld for both the lap shear and T-peel tests whereas pressure variations had the potential to change the weld category from good-weld to over-weld. However, time variation mostly helped to elevate the weld category from under-weld to good-weld within the investigated time boundaries.

Table 3: Effect of input parameter variations on weld category.

Input parameter variation		Weld category as per lap shear test	Weld category as per T-peel test
Amplitude (Constant- Pressure: 1 bar, Time: 0.60 sec)	40 µm	Under-weld	Under-weld
	45 µm	Good-weld	Under-weld
	50 µm	Good-weld	Under-weld
	55 µm	Good-weld	Good-weld
Pressure (Constant- Amplitude: 50 µm, Time: 0.60 sec)	1 bar	Good-weld	Under-weld
	2 bar	Good-weld	Good-weld
	3 bar	Over-weld	Good-weld
	4 bar	Over-weld	Over-weld
Time (Constant- Amplitude: 50 µm, Pressure: 1 bar)	0.15 sec	Under-weld	Under-weld
	0.30 sec	Under-weld	Under-weld
	0.45 sec	Good-weld	Under-weld
	0.60 sec	Good-weld	Under-weld

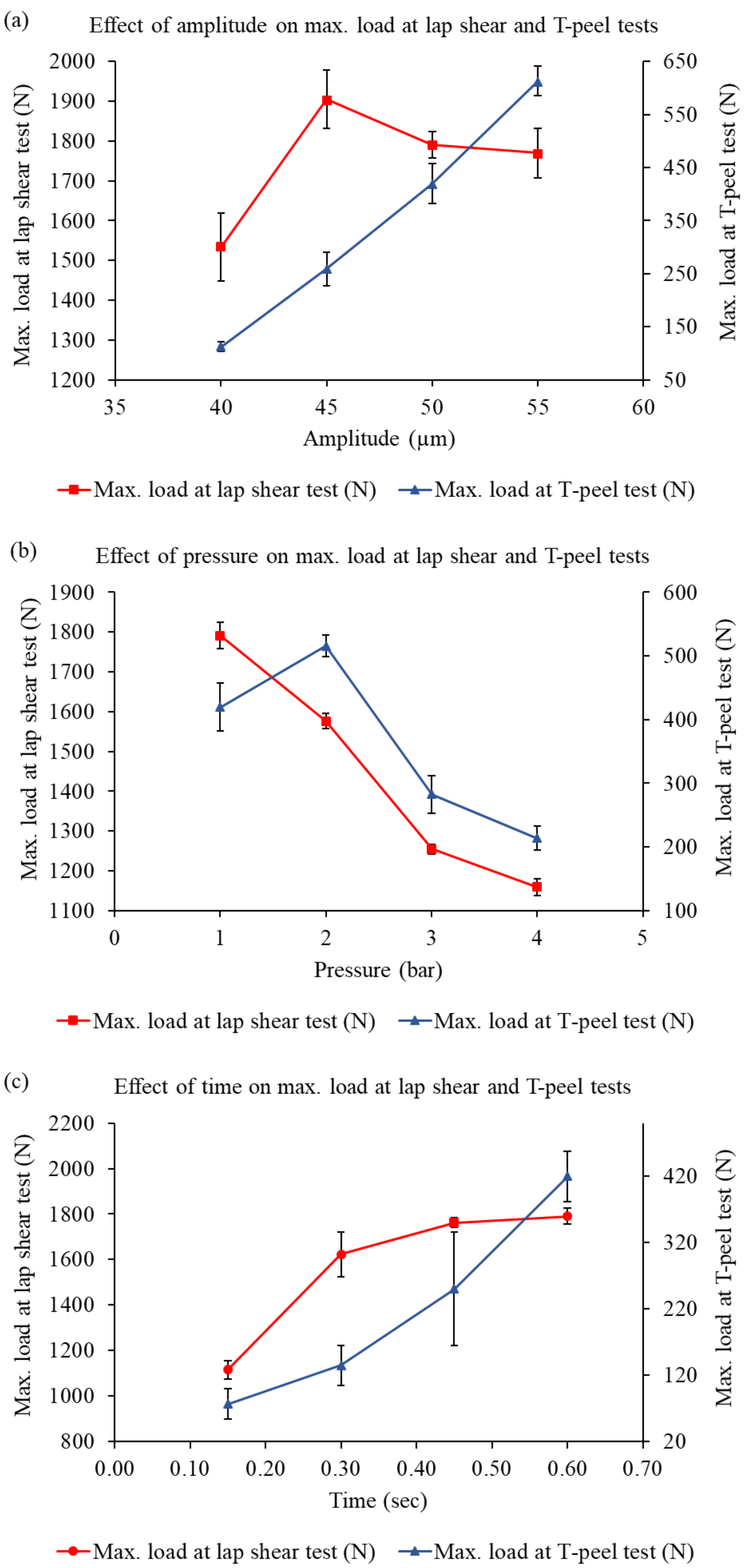

Fig. 2: Effect of (a) amplitude, (b) pressure and (c) time on maximum load obtained from the lap shear and T-peel tests.

3.2 Effect of process parameters on weld microstructure

Study of weld microstructure is an effective method to understand the overall weld mechanism and effect of different weld parameters on weld quality. In this work, the effects of the three weld parameters on the weld quality and weld mechanism were studied by critically observing the weld microstructure. The observed weld parameters were amplitude, pressure and time.

3.2.1 Effect of amplitude

To evaluate the effect of amplitude, it was varied from 40 µm to 55 µm by a step of 5 µm at a time while the other input parameters were kept at fixed values as shown in Table 2. Amplitude played an important role in multi-layered welding of dissimilar joints as depicted in Fig. 3a-d. It was prominent that the interfacial gaps at Al-Al interface 1, Al-Al interface 2 and Al-Cu interface were diminished with higher amplitude. The Al layers were not fully welded together when the amplitude was 40 µm (Fig. 3a). In addition, there was a gap in between the Al-Cu interface (Fig. 3a). When the amplitude was increased to 45 µm, these gaps between two subsequent Al layers were minimised (Fig. 3b). The Al_{top} and Al_{middle} layers were welded together in some places whereas gaps were visible at intermediate locations. However, the gap at Al-Al interface 2 was minute (Fig. 3b). For the other two amplitudes (i.e. 50 µm and 60 µm), there was no visible gap at Al-Al interface 1, Al-Al interface 2 and Al-Cu interface (Fig. 3c-d).

For further characterising the weld category, the post-weld thickness was studied for all the amplitude variations, which is shown in Fig. 4. The percentage of post-weld thickness was calculated by taking the ratio of the actual measured post-weld thickness to the sum of the initial thickness of Al layers. Then, the percentage of post-weld thickness was split into five categories as indicated in Fig. 4 and these divisions were made by analysing the lap shear and T-peel test data as depicted in Table 3. When the amplitude was at mid-levels (i.e. 40 µm and 45 µm), the post-weld thickness was varied in the range of 85% to 100% and the welds belonged to the category of under-weld. As the amplitude increased to 50 µm and 55 µm, the post-weld thickness fell in the range of 70 % to 85%, which belonged within the under-weld to good-weld transition zone.

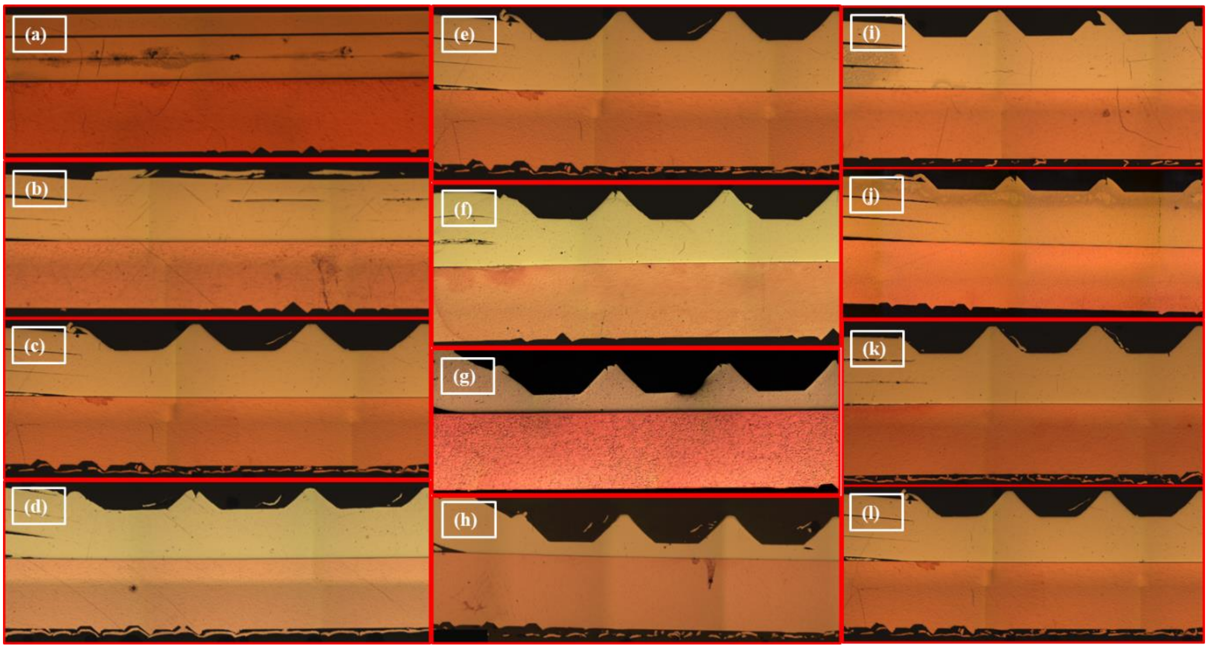

Fig. 3: Effect of input parameter variations on overall weld quality. Variation of amplitude: (a) 40 µm, (b) 45 µm, (c) 50 µm and (d) 55 µm when pressure: 1 bar and time: 0.60 sec; variation of pressure: (e) 1 bar, (f) 2 bar, (g) 3 bar and (h) 4 bar when amplitude: 50 µm and time: 0.60 sec; variation of time: (i) 0.15 sec, (j) 0.30 sec, (k) 0.45 sec and (l) 0.60 sec when amplitude: 50 µm and pressure: 1 bar.

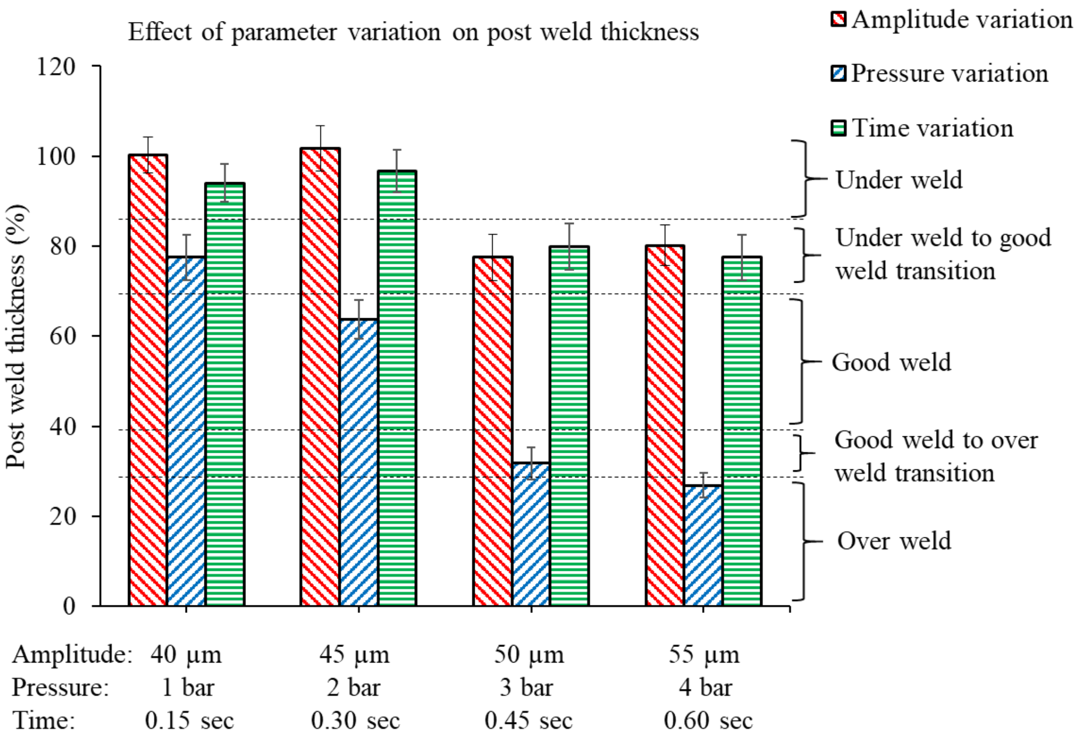

Fig. 4: Effect of input parameter variations on post-weld thickness.

3.2.2 Effect of pressure

The effect of pressure on welding was observed by varying the welding pressure from 1 bar to 4 bar with the incremental step of 1 bar. From the weld images in Fig. 3e-h, it was noticeable that all the Al layers were held together and there was no gap visible at the Al-Cu interface. In addition, there was no Al-Al interfacial joining layer visible as no gap resulted after the welding. It is worth noticing that the thickness of Al layers was reduced when the welding pressure was increased. This was further verified by analysing the post-weld thickness as shown in Fig. 4. At the pressure of 1 bar, the post-weld thickness was around 80% which was in the transition zone from under-weld to good-weld. When the pressure was increased to 2 bar, the post-weld thickness was reduced to around 60%. The range of good-weld lay in the region between 40% and 70% of the post-weld thickness. Hence, the weld at 2 bar pressure was in the good-weld category. However, a further increase in the pressure to 3 bar, the post-weld thickness remained in the zone of 30% to 40% and this zone was the transition from good-weld to over-weld. Similarly, when the pressure reached at 4 bar, the post-weld thickness was below 30% which was the lowest in the category and termed as over-weld.

3.2.3 Effect of time

Welding time was varied from 0.15 sec to 0.60 sec with an incremental step of 0.15 sec to visualise the effect of welding time on weld microstructure. Welding images (Fig. 3i-l) showed that there were no interfacial gaps in between two subsequent Al layers and at Al-Cu interface. In addition, there was no prominent weld line visible at the Al-Al layer interfaces. It was also noticeable that the Al layers were welded together and the combined thickness of Al layers was not varied much. Post-weld thickness graph (Fig. 4) revealed that time variation created a similar effect of amplitude variation. At the welding time of 0.15 sec and 0.30 sec, the weld category remained in the under-weld zone where the post-weld thickness was within 85% to 100%. On the other hand, when the welding time was at 0.45 sec and 0.60 sec, the welding belonged to under-weld to good-weld transition zone where the post-weld thickness was varied from 70% to 85%.

3.3 Microstructure based classification of weld categories

Visualising the joint formation is extremely crucial to understand the weld mechanism and the effects of the welding parameters. As there were three prominent weld categories, i.e. under-weld, good-weld and over-weld, the overall welding mechanism was analysed by observing these weld categories.

3.3.1 Under-weld

A typical optical micrograph of under-weld is shown in Fig. 5, which was obtained by using the input parameters as amplitude at 50 µm, pressure at 1 bar and time at 0.15 sec. Fig. 5d showed the weld micrograph with the Al layers and Cu layer where the Al layers were attached together and there was no gap visible at the Al-Al interfaces as well as at the Al-Cu interface when observing under the optical microscope at low magnification (i.e. 5x magnification). Optical micrographs at higher magnifications (i.e. 20x or 50x magnification) were carried out to investigate the interfacial gaps and interfacial material mixing.

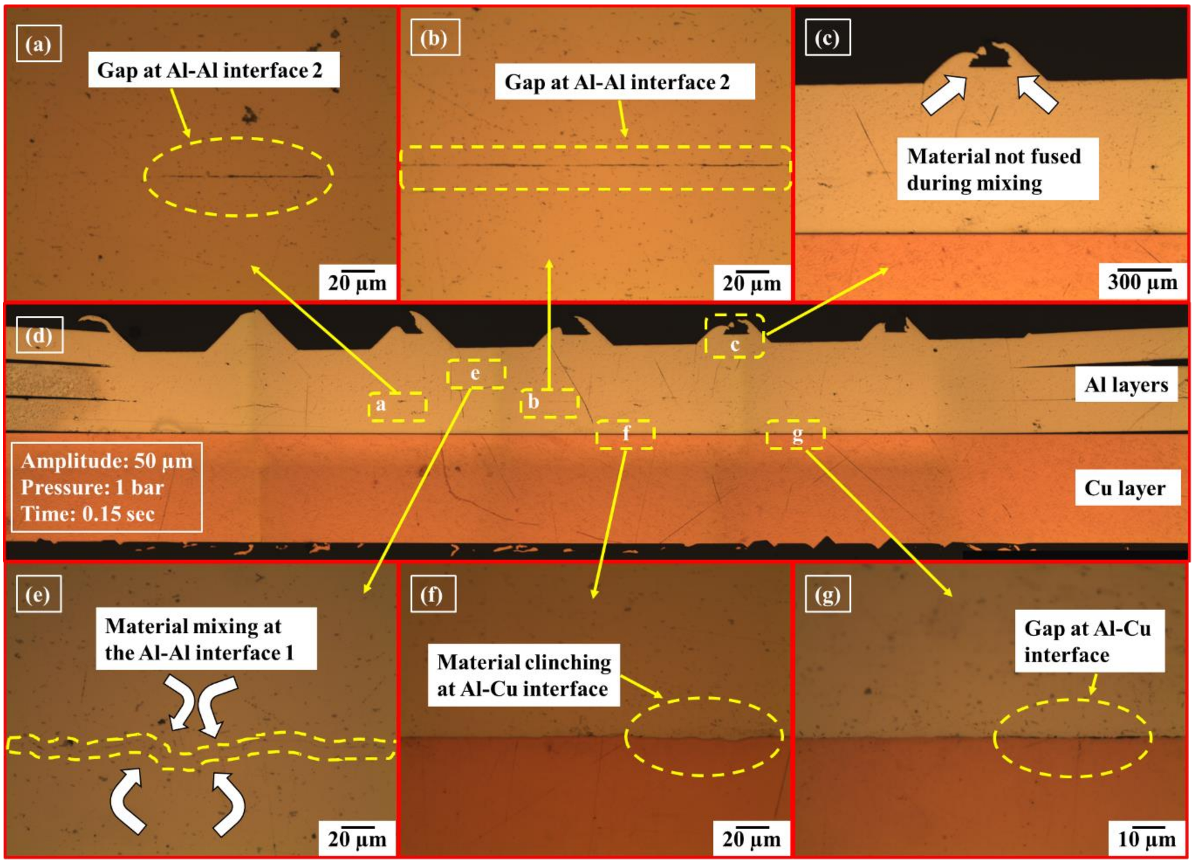

Fig. 5: Optical micrograph of a typical under-weld joint showing the welding mechanism.

Higher magnification revealed that there were gaps (surrounded by a dotted line) at Al-Al interface 2 and the Al-Cu interface (Fig. 5a, Fig. 5b and Fig. 5g). However, these gaps were not continuous. When the sonotrode tips applied the pressure on the Al layers during USW, the ongoing plastic deformation forced the material to flow (indicated by arrow) in order to fill the space in between two sonotrode tips (Fig. 5c). During under-weld, the flow of material was not sufficient to fill the space completely. Hence, there was a gap and material was not mixed or fused properly as shown in Fig. 5c. The plastically deformed material also helped to mix the materials at the two subsequent Al layers as well as at the Al-Cu interface. At the Al-Al interface 1, the material mixing was observed (indicated by arrow) and the micro-bonds, as well as wave-like interface [34], [35] (highlighted by the dotted line), was obtained (Fig. 5e). However, there was no gap observed at the Al-Al interface 1. On the other hand, the mixing of materials at the Al-Al interface 2 was not in higher intensity. Thus, there were intermittent interfacial gaps at the Al-Al interface 2 (surrounded by a dotted line in Fig. 5a and Fig. 5b). At the Al-Cu interface, material clinching, micro-bonds and wave-like interfaces [34], [35] (surrounded by a dotted line in Fig. 5f) were observed. However, at some portion, interfacial gaps or unbounded regions were observed (surrounded by a dotted line in Fig. 5g) as the ultrasonic energy input was not sufficient to create a continuous bond in under-weld.

3.3.2 Good-weld

Fig. 6 shows the typical micrograph of a good-weld. The welding parameters used to obtain the good-weld were amplitude at 50 µm, pressure at 2 bar and time at 0.60 sec. Any kind of interfacial (Al-Al and Al-Cu interfaces) gaps, cracks or unbonded regions were not observed in the lower magnification micrograph of optical microscope (Fig. 6d). Whereas higher magnification revealed many underlying features which helped to understand the joint behaviours. When the sonotrode tips plunged into the Al layers, the materials were plastically deformed and the material was started to flow in the space between two sonotrode peaks and eventually tried to be mixed and fused properly (indicated by arrows in Fig. 6b). However, there was a thin gap or unbonded line under the sonotrode valley region (inverted delta or crest) as indicated by the dotted circle in Fig. 6b and it shows that the material mixing and fusion were not perfect at few crests of the good-weld. The sonotrode vibration helped the plastically deformed materials to be mixed properly at the Al-Al interfaces (Fig. 6a, Fig. 6c and Fig. 6e) and Al-Cu interface (Fig. 6f-g) as indicated by a dotted line. The mixing of materials at the Al-Al interface 1 was so intense that no continuous interfacial line was visible at the interface. The material mixing is indicated by the arrows (Fig. 6a). On the other hand, a continuous interfacial line was observed at the Al-Al interface 2 (Fig. 6c and Fig. 6e). A close view at the interfacial line revealed that the line was not straight rather it was wave-like. These suggested that the micro-bonds and swirls along with the interface occurred due to severe material mixing (indicated by arrows in Fig. 6c and Fig. 6e). The effect of severe material mixing was also prominent at the Al-Cu interface (Fig. 6f and Fig. 6g). Furthermore, material clinching and micro-bonds were observed at the Al-Cu interface (surrounded by a dotted line in Fig. 6f and Fig. 6g) due to the material mixing and there was no gap at the interface. This wave-like interface of micro-bonds at Al-Cu interface confirmed that the good-weld was obtained [34], [35]. Also, the energy input for good-weld was higher than the under-weld.

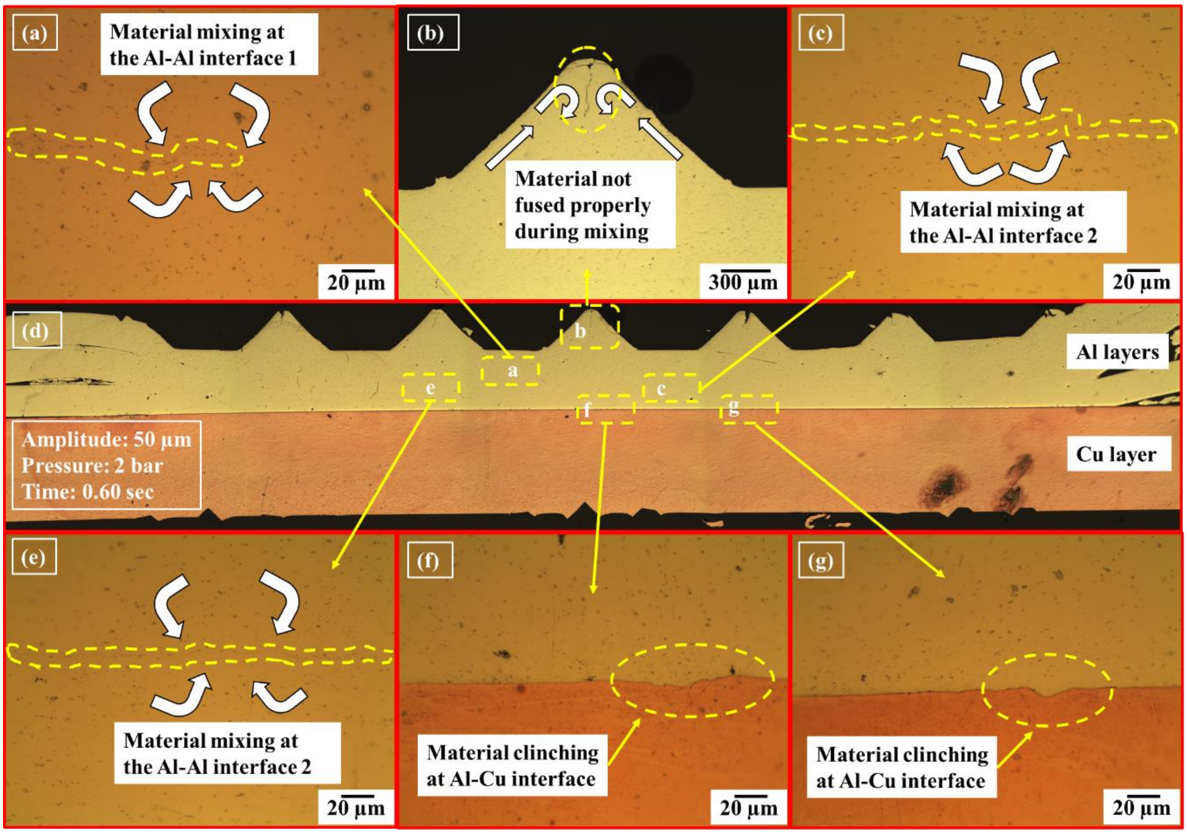

Fig. 6: Typical optical micrograph of a good-weld indicating welding mechanism.

3.3.3 Over-weld

A typical over-weld micrograph is presented in Fig. 7 where the Al layers and Cu layer are indicted in the micrograph. The welding parameters used to produce the over-weld were amplitude: 50 µm, pressure: 4 bar and time: 0.60 sec. From the optical micrograph (Fig. 7c) at lower magnification, no gaps, cracks or unbonded region were observed. Whereas, the thickness of the Al layers were reduced significantly after welding as compare to unwelded samples. Higher magnification micrograph showed the material mixing. Vibrational movement of the sonotrode helped the plastically deformed material to flow and fill the inter sonotrode tip spaces. As the sonotrode tips went further into the material, the mixing (indicated by arrows in Fig. 7b) was sufficient to fill the space between two sonotrode tips and fused properly (shown by a dotted circle in Fig. 7b). Hence, no gap or unbonded line was observed at the crests. As the plastic deformation and mixing of material were severe, no interfacial gap was noticed at the Al-Al and Al-Cu interfaces. In addition, any kind of crack was not present at the interfaces. The material mixing was so intense that there was no interface distinguished between Al_{top} and

Al$_{middle}$ layers (Fig. 7e). On the other hand, there were small segments of discrete interfaces (indicated by a dotted line in Fig. 7a) were observed at the Al-Al interface 2. In other locations, the material mixing was very high (shown by arrows in Fig. 7a) and hence, no interfacial line was revealed. Whereas, the material clinching and micro-bonds (indicated by a dotted line in Fig. 7d) were extremely prominent at the Al-Cu interface. Furthermore, the micro-bonds formed a wavy interface layer [34], [35] (highlighted by dotted area in Fig. 7f) which showed the high material mixing characteristic of over-weld. In addition, the energy input to the over-weld was the highest among all the weld categories.

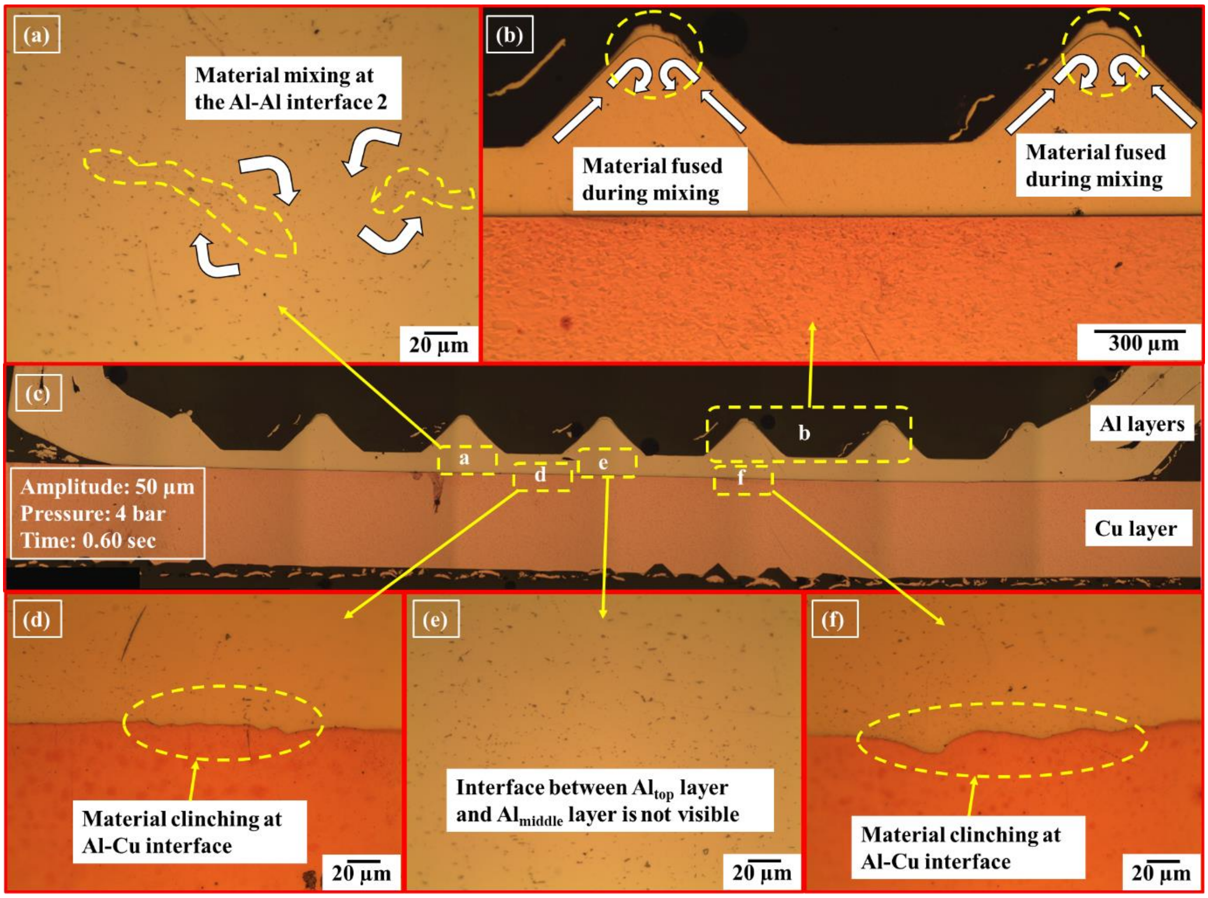

Fig. 7: Optical micrograph of a typical over-weld elucidating the welding mechanism.

3.4 Micro-hardness distribution

To characterize work hardening and softening phenomena, Vickers micro-hardness test was carried out on the polished surface of the weld cross-section to evaluate the micro-hardness profile of the under-weld, good-weld and over-weld categories. Due to high plastic deformation, the average micro-hardness under the sonotrode peak for all the weld categories is presented in Fig. 8. In under-weld, the average micro-hardness under sonotrode peak was increased by 8% than the as-received material micro-hardness (40 HV) due to a large amount of cold work or work hardening. On the contrary, the micro-hardness values for the good-weld and over-weld were measured around 23% and 28% below the as-received material respectively. The reason for this was the heat generation and subsequent thermal softening process during the welding operation. In order to construct a layer-wise two-dimensional micro-hardness map of the Al layers, the micro-hardness distribution was evaluated along (i) horizontal direction and (ii) vertical direction.

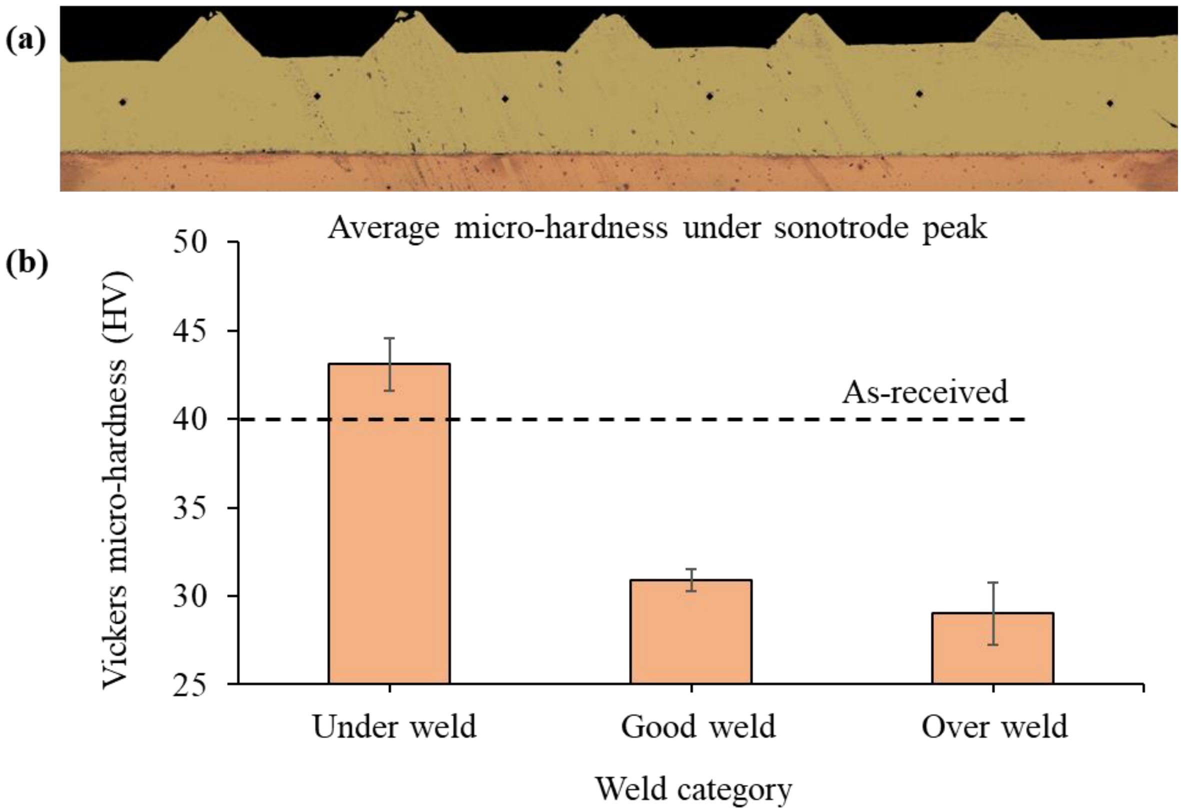

Fig. 8: (a) Locations of Vickers indentation during micro-hardness measurement and (b) average micro-hardness under sonotrode peak for under-weld, good-weld and over-weld.

3.4.1 Layer-wise two-dimensional micro-hardness map

The micro-hardness distribution along horizontal and vertical directions for each layer of Al are shown in Fig. 9 and Fig. 10 respectively for all weld categories i.e. under-weld, good-weld and over-weld. For horizontal micro-hardness map, the micro-hardness was measured only at crests (i.e. formed at sonotrode valley) in Al_{top} layer, whereas for the other two layers (i.e. Al_{middle} and Al_{bottom}), micro-hardness values were calculated at the regions under both the peak and valleys of sonotrode (see Fig. 9a). In case of vertical micro-hardness map, micro-hardness measurement points are shown in Fig. 10a representing the average micro-hardness for each layer to demonstrate the propagation of plastic deformation and thermal softening behaviour. When the sonotrode tips impinged on the material surface, the materials started to flow towards the sonotrode valley position and created crest (an inverted delta shape) as shown in Fig. 9a and Fig. 10a. Fig. 9b shows the micro-hardness variation of Al_{top} layer along the horizontal direction for three weld categories. It was observed that the micro-hardness at the Al_{top} layer for under-weld was slightly higher than the other two weld categories. Micro-hardness variation at the Al_{middle} layer along the horizontal direction is depicted in Fig. 9c for all the weld categories. As the sonotrode peaks impinged on the metal surface during USW, the plastically deformed material moved towards the sonotrode valley locations as well as the Al-Cu interface. However, for the under-weld, the material was not fused properly below the Sonotrode valley and at the Al-Cu interface while producing unfused zone and interfacial gaps as described in section 3.3.1. Hence, the material at the Al_{middle} layer was affected most than Al_{top} and Al_{bottom} layers in term of work hardening intensity and thus, the Al_{middle} layer had higher micro-hardness (see Fig. 9c and Fig. 10b) due to the severe cold work occurred during plastic deformation. On the contrary, the micro-hardness of all the peaks and valleys at the Al_{middle} layer for the good-weld and over-weld were below the as-received micro-hardness due to thermal softening. For the good-weld, micro-hardness at Al_{middle} layer was a little higher than that of over-weld as the extent of thermal softening was greater in case of over-weld. The horizontal variation of micro-hardness distribution at the Al_{bottom} layer is shown in Fig. 9d. The micro-hardness of the under-weld joint revealed that its values under sonotrode peaks were higher than that of the valleys. This was observed due to the fact that the plastic deformation was started at the sonotrode tip when the sonotrode peak was impinged on the Al_{top} layer and subsequently it extended outwards as the ultrasonic weld proceeds. Hence, the area under sonotrode peaks was more work-hardened than the valleys [6], [17]. However, this difference in micro-hardness values at sonotrode peaks and valleys at the Al_{bottom} layer of the good-weld and over-weld was relatively low due to the thermal softening [6], [17]. Moreover, the Al_{bottom} layer was more thermally softened than the Al_{top} layer. Hence, the micro-hardness of the Al_{bottom} layer was much less than that of the Al_{top} layer. Similar observations were obtained from the average micro-hardness values along the vertical direction for all the weld categories as indicated in Fig. 10b.

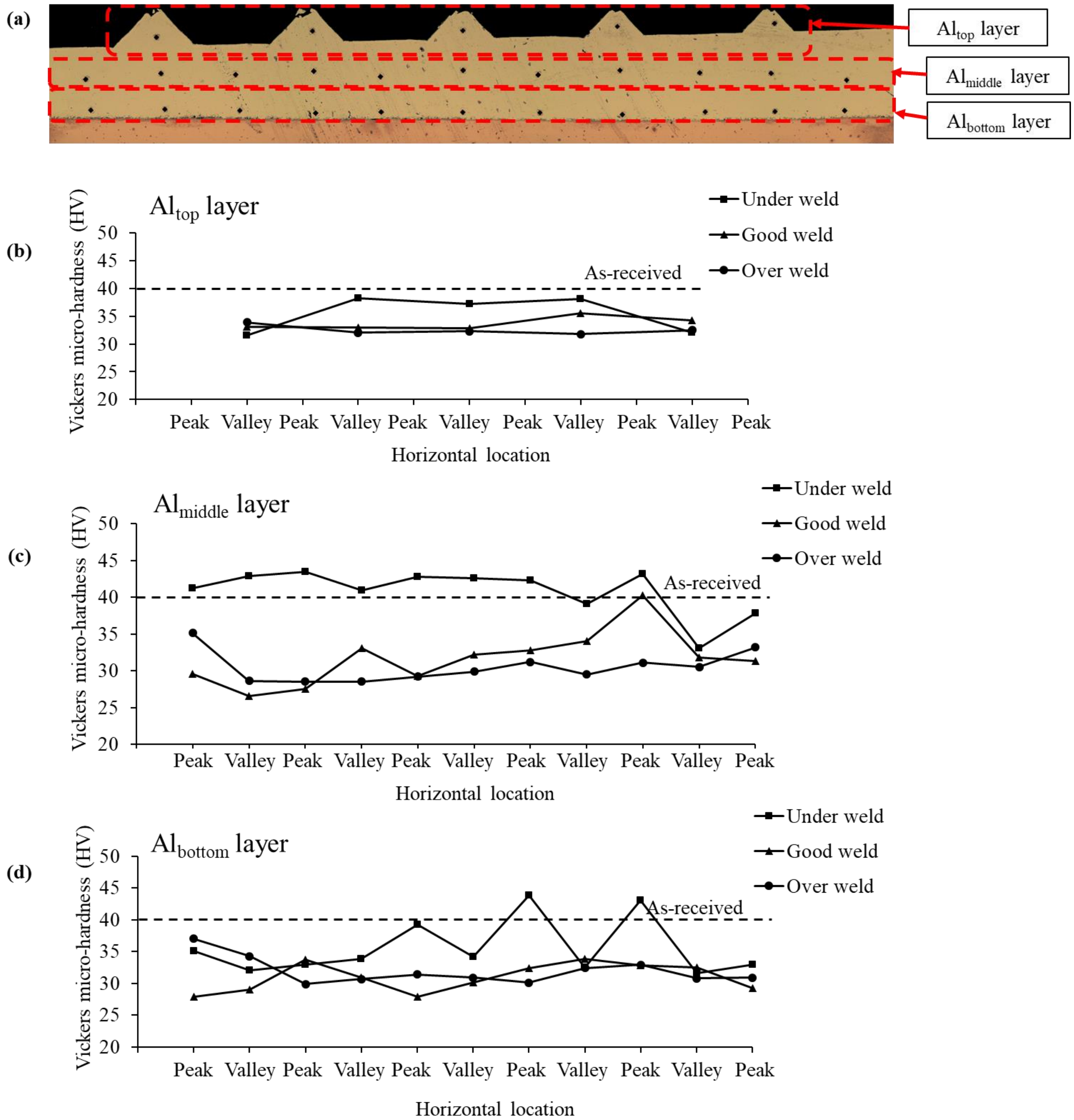

Fig. 9: Micro-hardness profile along the horizontal direction indicating micro-hardness at each Al layers: (a) locations of Vickers indentation, (b) micro-hardness at the Al$_{top}$ layer, (c) micro-hardness at the Al$_{middle}$ layer and (d) micro-hardness at the Al$_{bottom}$ layer.

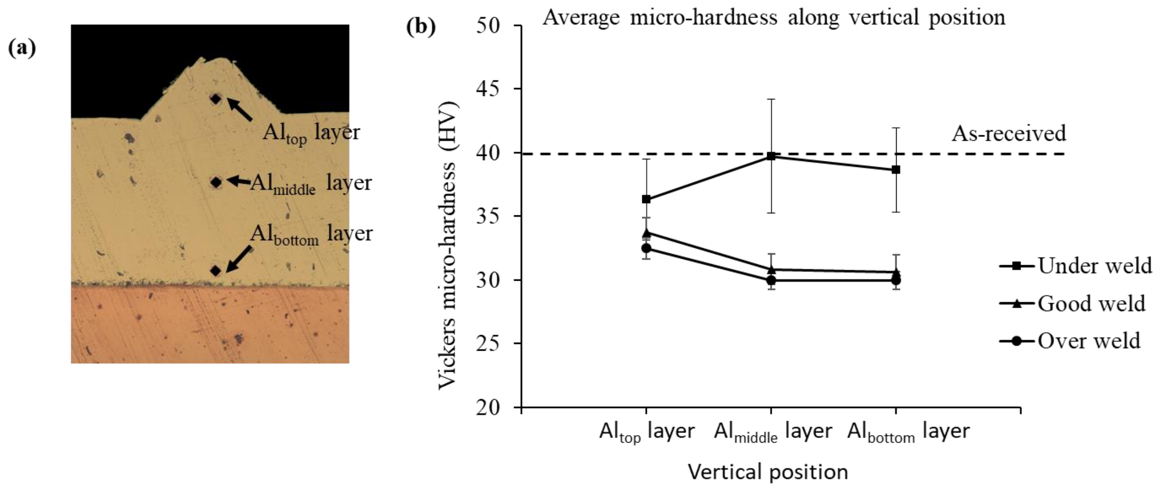

Fig. 10: Micro-hardness variation along vertical direction: (a) locations of Vickers indentation and (b) average micro-hardness along with the vertical position for all weld categories.

3.4.2 Micro-hardness profile outside of weld zone

Micro-hardness profiles outside of weld zone of different weld categories namely under-weld, good-weld and over-weld were measured and are presented in Fig. 11. To create the micro-hardness profile outside the weld nugget, the Vickers indentations were made after every 0.15 mm distance starting from the Al-Cu interface and continued until 4.35 mm along the midplane of the Al$_{top}$ layer (Fig. 11a). Fig. 11b shows the variation in micro-hardness profiles for different weld categories. The micro-hardness variation confirmed that each weld category had experienced a different pattern of work hardening and thermal softening. It was evident that, for the under-weld, the micro-hardness was below the as-received micro-hardness at the Al-Cu interface and it was rapidly increased (40% increase) to maximum micro-hardness near the weld zone boundary (around 1 mm from the Al-Cu interface). Thereafter, the micro-hardness values were reduced and settled down near as-received micro-hardness value. In case of the good-weld and over-weld, the highest micro-hardness value shifted further away from the weld zone boundary. For good-weld and over-weld specimens, the micro-hardness at the Al-Cu interface was below the as-received micro-hardness and it was increased likewise and finally reached to the maximum micro-hardness at two different distance from the weld zone. In case of good-weld, it was around 1.5 mm from Al-Cu interface while in over-weld specimen it was nearly at 2 mm from Al-Cu interface. Both these distances were far from the weld zone boundary. After the maximum micro-hardness, both good-weld and over-weld specimens maintained steady micro-hardness similar to the as-received micro-hardness value. The high micro-hardness value away from weld zone was caused by the plastic deformation and cold work due to the cyclic stresses exerted by ultrasonic vibration (horizontally) and clamping force (vertically) during the USW process [6], [17]. However, for the good-weld and over-weld, the decrease of micro-hardness at the weld zone was due to the thermal softening associated with temperature rise. Hence, the regions outside of weld zone for good-weld and over-weld were thermally and mechanically affected by USW process.

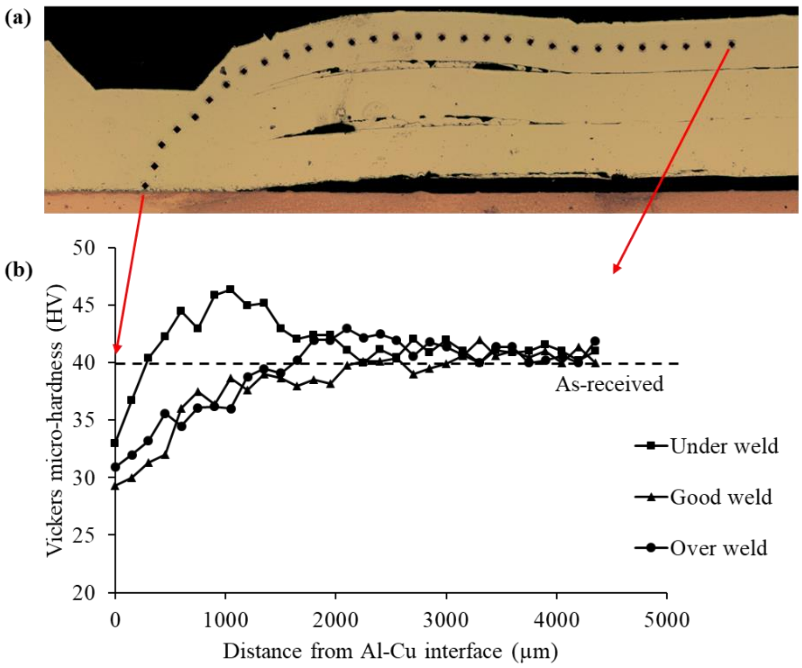

Fig. 11: Micro-hardness profile outside of weld zone: (a) micrograph containing micro-hardness indentation marks and (b) Vickers micro-hardness profile of three different weld categories.

3.5 Study of grain formation and recrystallization

Grain formation within the weld zone of different weld categories was studied using electron back scattered diffraction (EBSD) orientation mapping to understand the deformation, bonding and recrystallization during USW. A representative slice of full EBSD orientation map obtained at the centre of a typical good-weld is shown in Fig. 12.

The EBSD micrographs of Al sheet and Cu sheet are shown in Fig. 12a and Fig. 12b respectively before the welding. The average grain size observed at the Al sheet before welding was around 18 μm. The full EBSD orientation map is shown in Fig. 12c whereas the various region of interests are shown in Fig. 12d-f. The crest (Fig. 12d) was formed due to the material flow (indicated by yellow dotted lines) from the region beneath the sonotrode peaks to fill the space beneath the sonotrode valleys. The movement of the material rendered the grains to become elongated (Fig. 12d). The EBSD data of the region beneath the sonotrode peak revealed that there were three distinct zones observed in the Al layers of the Al-Cu weld (Fig. 12e): (i) a severely deformed region of fine grains (~5μm) close to the Al-Cu interface named as interface zone; (ii) a forged zone beneath the sonotrode tips, where the topmost Al sheet layer had been largely deformed as a result of compression when the sonotrode tips had sunk into the material and subsequently, softened due to the temperature rise; and (iii) an intermediate region where distinct evidence of plastic deformation was found and elongated grains were visible [19]. The Al-Cu interface region is shown in Fig. 12f. The grains near the Al-Cu interface were fine (~5μm) whereas the grains far from the Al-Cu interface were relatively coarse (~13μm) in nature.

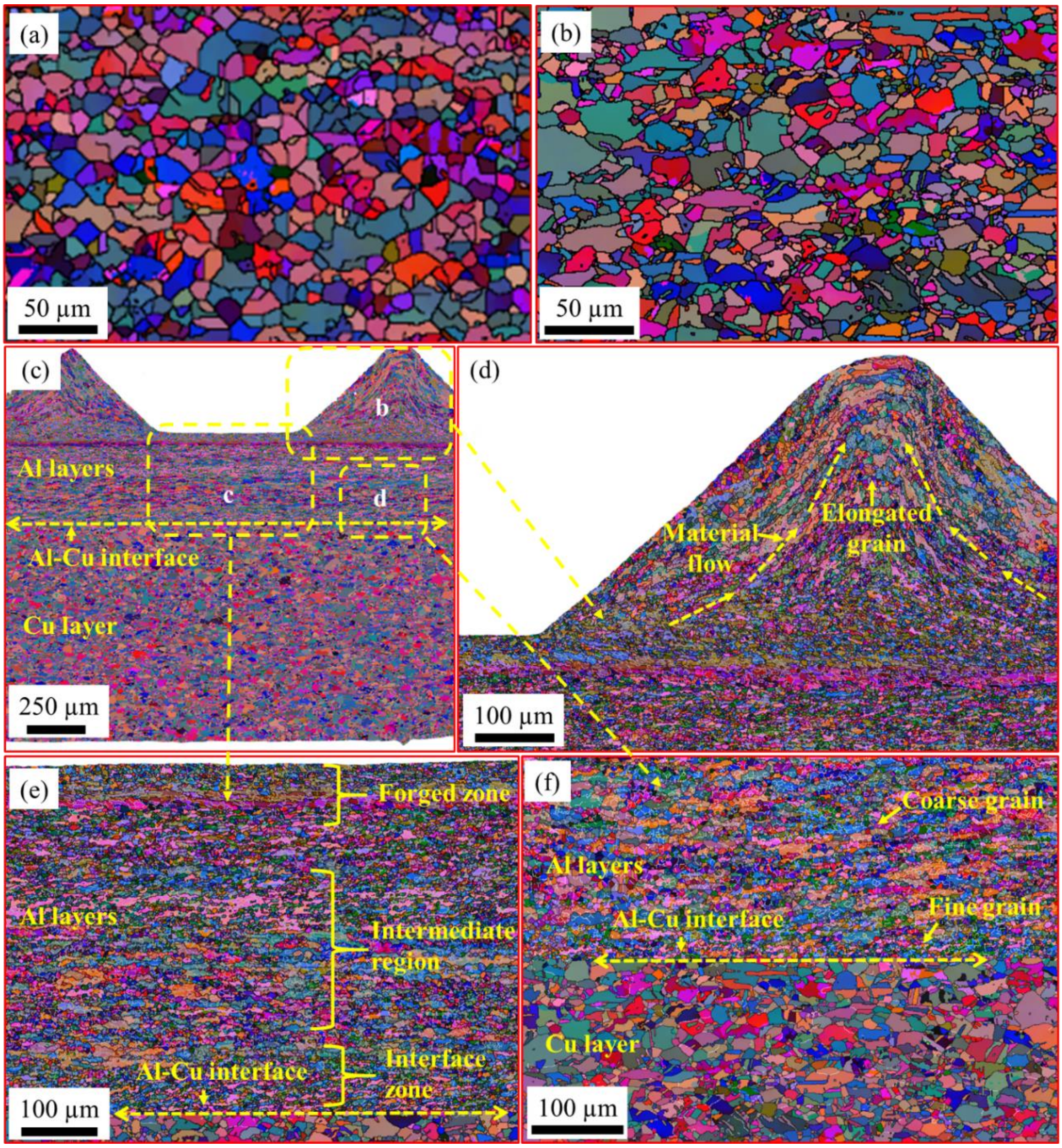

Fig. 12: EBSD micrograph (Euler contrast) of (a) Al sheet and (b) Cu sheet before the welding. High resolution EBSD orientation maps (Euler contrast) of good-weld indicating: (c) a typical slice at the centre of weld zone, (d) the crest, (e) material beneath the sonotrode peak and (f) Al-Cu interface region.

The comparison of three different weld locations named as (i) the crest, (ii) Al layers under the sonotrode tips and (iii) Al-Cu interface of all the weld categories are depicted in Fig. 13. The pattern of material mixing during the formation of the crest of under-weld was different from the pattern in good-weld and over-weld (Fig. 13a-c). During under-weld, the material was flowing towards the crest from the region under the sonotrode peaks as well as from the region in between two subsequent peaks as shown in yellow dotted line in Fig. 13a. The material movement during the formation of the crest in good-weld and over-weld is shown in yellow dotted line in Fig. 13b-c respectively. The Al layers of under-weld, good-weld and over-weld under the sonotrode peaks are shown in Fig. 13d-f that portrayed the evidence of plastic deformation in the material compressed during the welding process. In under-weld, three Al layers were prominently observed (Fig. 13d) and the Al_{top} layer was severely deformed whereas other two layers (i.e. Al_{middle} and Al_{bottom} layers) were less deformed. The total weld energy applied during the weld formation was relatively less for under-weld than the other two weld categories. Therefore, this insufficient energy was able to mostly deform the Al_{top} layer leaving the other two layers relatively less deformed. The shear band could also be found in the Al_{top} layer indicating the direction of material flow. In between any two Al layers, a thin layer of fine grains was observed. This layer of fine grains was observed due to the intermixing of the material from the top and bottom Al layers. In good-weld and over-weld, the Al layers were mixed properly and represented as a single layer (Fig. 13e-f). Hence, the individual layers were not prominent. The grains were more elongated in over-weld than good-weld as higher energy was put into the material during the material compression. The compressed layer thicknesses of good-weld and over-weld were measured around 400 µm and 100 µm respectively.

In the Al-Cu welds, the grain structure of Cu sheet, as evident from the EBSD orientation mapping, was virtually identical for all weld categories (Fig. 13g-i). Hence, the induced deformations during the USW process were mostly confined within the Al layers. In the under-weld Al layers, a thin band of ultrafine (~3µm) grains was observed at the weld interface (Fig. 13g). However, the grain size rapidly increased and elongated (~26µm) and furthermore, the density of high angle (>15°) grain boundaries (HAGB) was decreased with distance from the Al-Cu interface, even though a relatively high density of low angle (<15°) grain boundaries (LAGB) was still observed far from the Al-Cu interface [19]. This suggested that less deformation was occurred at the middle portion of each Al layers (i.e. Al_{top}, Al_{middle} and Al_{bottom}) in under-weld (Fig. 13g). In good-weld, aluminium grains at the Al-Cu interface became slightly larger (~5µm) (Fig. 13h), and the density of HAGBs was decreased. In contrast, number of HAGBs was increased and LAGBs were decreased when they were measured away from the Al-Cu interface. For the over-weld, the grain structure within the aluminium side of the weld became more uniform and equiaxed (average grain size ~9µm), indicating that recrystallization had occurred (Fig. 13i) [18]. Furthermore, the number of HAGBs and LAGBs was decreased within the over-weld (Fig. 13i).

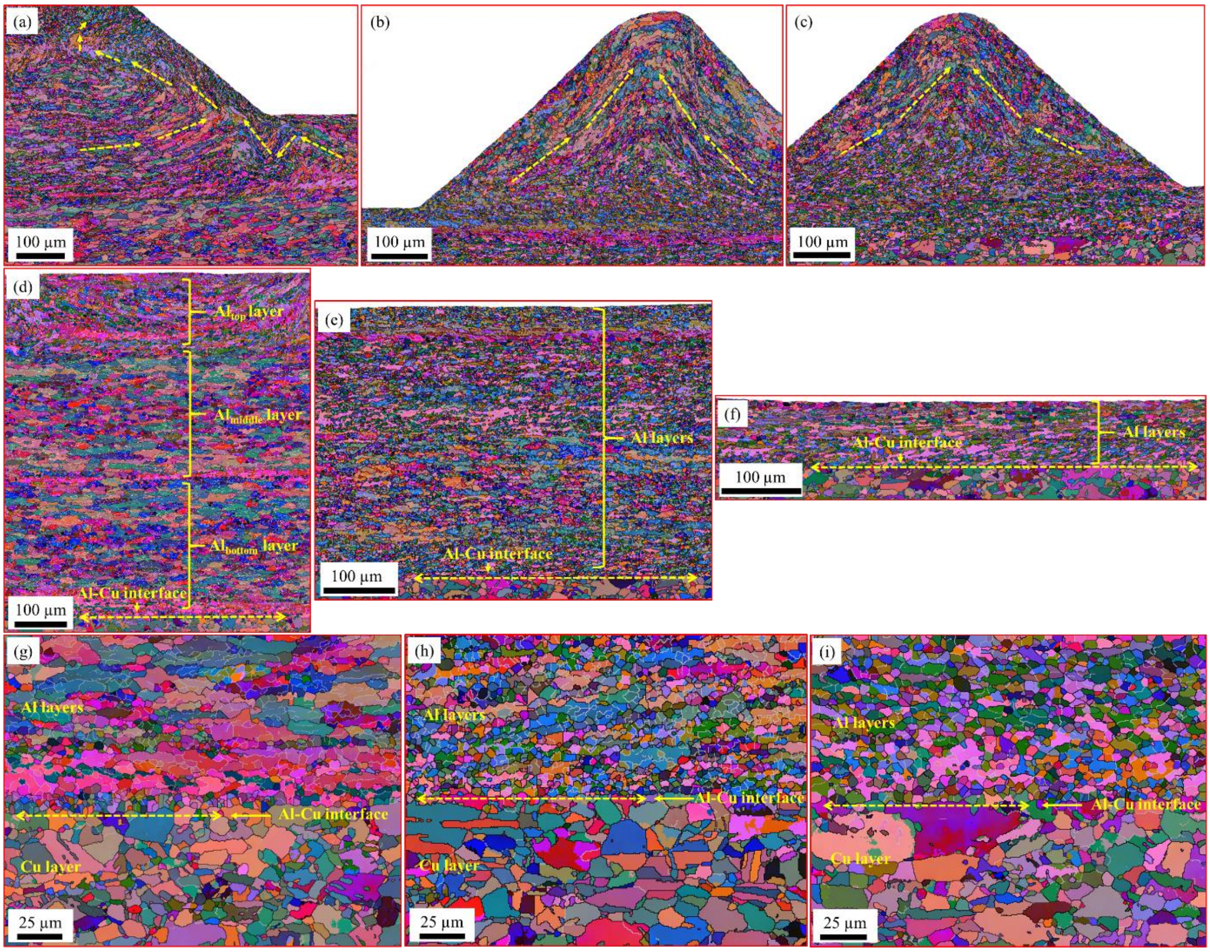

Fig. 13: High resolution EBSD orientation maps (Euler contrast) of the crest (a-c), Al layers under the sonotrode peak (d-f) and Al-Cu interface (g-i) of under-weld (a, d, g), good-weld (b, e, h) and over-weld (c, f, i) respectively. High angle grain boundaries (>15◦) are shown by dark lines and low angle grain boundaries (<15◦) by light grey lines.

3.6 Fractography analysis

Typical SEM images of tensile lap shear fracture surfaces of under-weld, good-weld and over-weld of dissimilar Al-Cu joints are illustrated in Fig. 14, Fig. 15 and Fig. 16 respectively. In the lap-shear tensile tests, the welds were generally fractured along the weld interface of the under-weld (Fig. 14a-b), while fracture occurred at the circumference of the weld (nugget pull out) in over-weld [36] (Fig. 16a-b). The failure mode in good-weld was partial nugget pull out with material sticking at the weld interface (Fig. 15a-b). It can be seen from Fig. 14 that whole fracture surface is flat in the under-weld with some trace of Al attached to Cu surface. The higher resolution images of the yellow-boxed areas in Fig. 14 shows that the attached material with the fracture surface is very little and not covering the entire weld surface. As this little amount of material did not provide sufficient resistance during the lap shear test, the weld strength was not high in under-weld. In contrast, a characteristic dimple-rupture failure mode [36] was found in good-weld as shown in Fig. 15. The dimples provided sufficient strength [37] during the lap shear test and as a result, the highest weld strength was observed in good-weld. On the other hand, the fracture mode observed in over-weld (Fig. 16) was mainly a ductile fracture. As the nugget pull out was observed in the over-weld, only the periphery of the weld was prone to ductile fracture. Hence, the weld strength was lower than good-weld but much higher than under-weld.

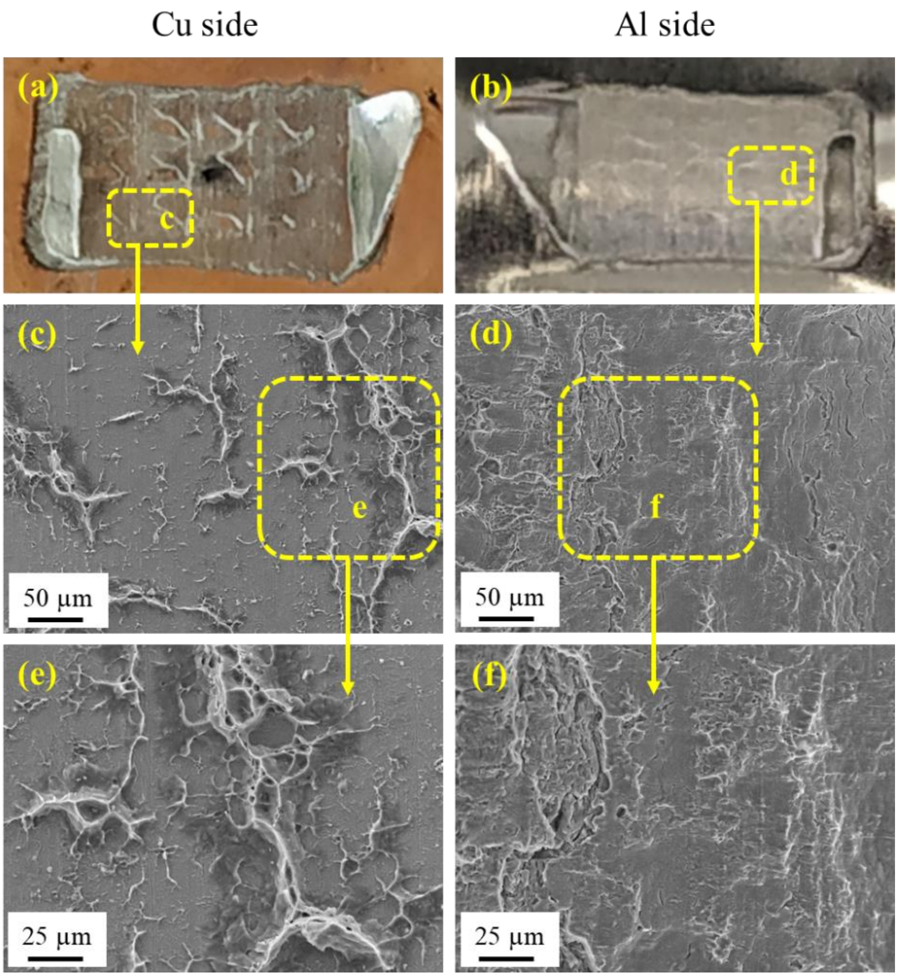

Fig. 14: Typical SEM images of tensile lap shear fracture surfaces of under-weld: (a) overall view of Cu side, (b) overall view of Al side, (c) magnified image of the box in (a), (d) magnified image of the box in (b), (e) magnified image of the box in (c), and (f) magnified image of the box in (d) revealing fracture along with the interface.

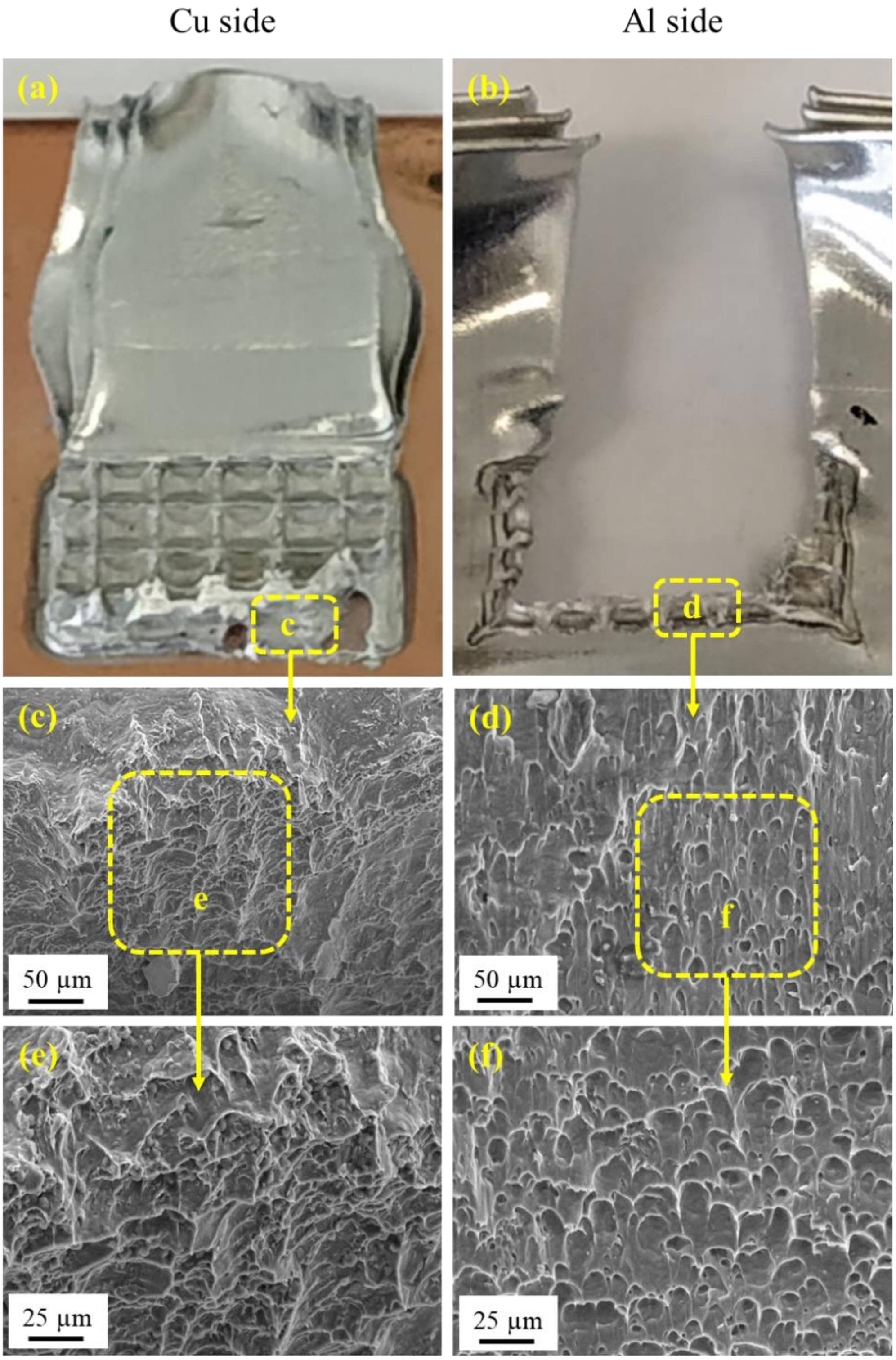

Fig. 15: Typical SEM images of tensile lap shear fracture surfaces of good-weld: (a) overall view of Cu side, (b) overall view of Al side, (c) magnified image of the box in (a), (d) magnified image of the box in (b), (e) magnified image of the box in (c), and (f) magnified image of the box in (d) showing dimple like fracture.

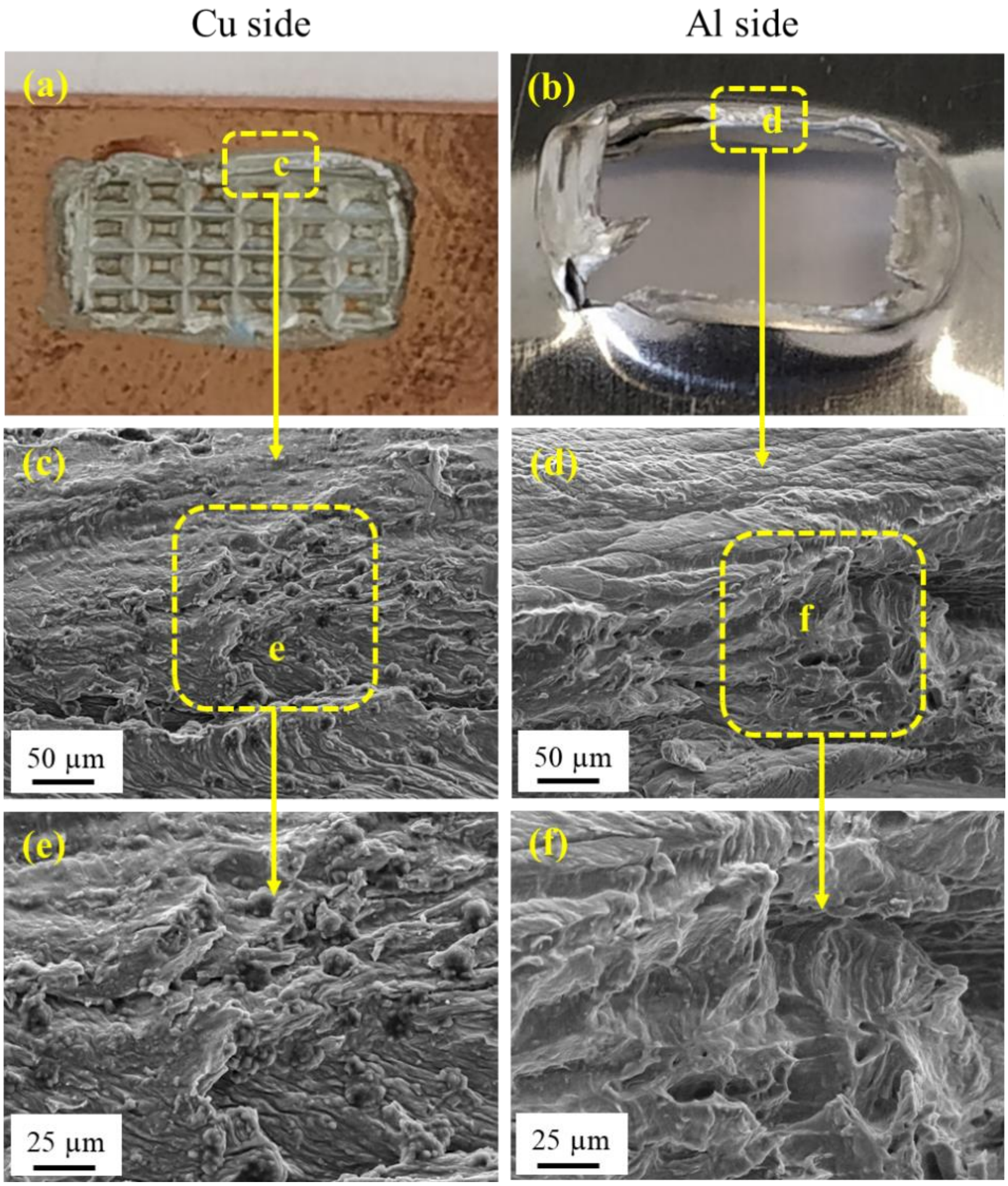

Fig. 16: Typical SEM images of tensile lap shear fracture surfaces of over-weld: (a) overall view of Cu side, (b) overall view of Al side, (c) magnified image of the box in (a), (d) magnified image of the box in (b), (e) magnified image of the box in (c), and (f) magnified image of the box in (d) conforming ductile fracture.

4 Discussion

The welding mechanism in USW is a complex process where ultrasonic vibration causes cyclic deformation by applying low amplitude and high-frequency vibration with the help of high pressure [21]. Generally, the deformation during USW is mainly confined at the weld line and the bonding mechanism is mainly dominated by interfacial micro-bonds formation arising after the break-up of the interfacial oxide layer [21]. Application of continuous pressure and vibration raises the temperature at the interface to such an extent that it becomes sufficiently soft to undergo plastic deformation and intermixing happens at the weld line [21]. The input parameters i.e. welding pressure, welding time and amplitude of ultrasonic vibration play a significant role in the bonding mechanism [38]. In this study, the weld strength was measured by the lap shear test and T-peel test. The attainment of higher weld strength was associated with a transition from weld interface failure to weld nugget pull out [21]. The higher weld strength was achieved at an optimum range of weld energy when plastic deformation expanded to the whole weld zone, rather than just at the weld interface, resulting in a macroscopic wave-like material clinching at the interface [21].

4.1 Effect of input parameters on weld strength

Welding parameters have the potential to change the weld strength as welding parameters control the overall energy input to the weld. In this study, the effects of amplitude, pressure and time were studied on weld strength in term of maximum loads obtained from lap shear and T-peel tests.

4.1.1 Lap shear strength

Lap shear strength was mainly influenced by pressure and time as described in section 3.1. However, during the amplitude variation the weld energy was varied from 310 J - 790 J (Table 2), the amplitude variation did not produce a similar effect in comparison with the time variation (Fig. 2) (weld energy varied from 111 J - 615 J) (Table 2). Generally, when the weld energy was below 400 J, under-weld was produced. Good-weld was produced in the typical range of 400 J - 700 J and over-weld was obtained above 700 J (Table 2 and Table 3). During amplitude variation, weld energy was varied from under-weld to over-weld zone, the weld strength did not change much (within 20% of lap shear strength). Hence, amplitude variation was not an effective way to alter the weld strength in term of lap shear strength when the weld energy was in between 300 J - 800 J. This may be attributed to the weld energy where the amplitude of vibration was not fully transmitted to the weld material and there might be loss of vibrational energy, which did not fully convert to the heat generated at the weld interface.

On the other hand, time variation had a prominent effect on weld energy. During time variation, the weld energy was varied from 111 J to 615 J, which was ranging from under-weld to good-weld (Table 2 and Table 3). Within this range of weld energy, the higher welding time was favourable for the weld strength (Fig. 2c). As the time was increased, the weld interface got time to be heated up and plastically deformed the material at the weld interface as well as under the sonotrode tip. It got favourable time to mix properly and recovery of the deformed grains helped to produce a sound weld.

During pressure variation, the weld energy was varied from good-weld to over-weld (615 J – 741 J) (Table 2 and Table 3). In this range of weld energy, lower pressure was favourable (Fig. 2b) as high pressure deformed the weld material to a great extend which hindered the flow of plastically deformed material and the sonotrode tips drastically plunged into the material which did not give much space of the plastically deformed material to flow under the sonotrode valley regions. However, sufficient pressure was required to plunge the sonotrode into the weld material, otherwise the plastically deformed material could not reach the sonotrode valley regions and may lead to under-weld.

Overall, weld energy in the range of 400 J - 700 J and amplitude in the range of 45 µm - 50 µm, lower pressure (1 bar - 2 bar) and higher time (0.45 sec - 0.60 sec) would lead to good-weld strength in term of lap shear test. Time was the most critical parameter than pressure and amplitude.

4.1.2 T-peel strength

T-peel strength was affected by all the three welding parameters namely amplitude, pressure and time in this study as reported in section 3.1. According to T-peel strength, weld energy below 650 J produced under-weld while weld energy in between 650 J - 740 J produced good-weld and above 740 J produced over-weld (Table 2 and Table 3). During the amplitude variation, weld energy varied from under-weld to good-weld (310 J – 790 J) (Table 2 and Table 3). In this range of weld energy, the higher amplitude was favourable for good joint formation (Fig. 2a). The amplitude should be high enough so that the vibrational loss was compensated and a good amount of vibrational energy was transmitted to the weld zone. On the other hand, pressure should be low to moderate in order to produce good joint (Fig. 2b). During pressure variation in this study, the weld energy varied in the range of under-weld to over-weld (615 J

– 741 J) (Table 2 and Table 3). The pressure should be low but sufficient for pushing the sonotrode tips into the metal so that there should be sufficient area the plastically deformed material can travel and mix properly. High pressure was detrimental, as it did not give the softened material sufficient space to flow and mix properly. During time variation, weld energy varied from 111 J – 615 J (Table 2 and Table 3) that belonged to weld categories covering under-weld to good-weld. In this range, higher time was necessary (Fig. 2c) for the plastically deformed material to flow and mix properly. Otherwise, the mixing would not be proper if the time was less and it might lead to void formation at the weld interface and gap formation under the sonotrode peaks.

Hence, keeping weld energy in the range of 650 J - 740 J and pressure in the range of 1 bar - 2 bar, higher amplitude (50 µm - 55 µm) and higher time (0.45 sec - 0.60 sec) would lead to good-weld in term of weld strength measure by T-peel test. Time was the most critical parameter than pressure and amplitude.

4.2 Study of weld formation for three weld categories

In this work, three layers of 0.3 mm Al sheet were welded with a single layer of 1.0 mm Cu layer for multi-layered USW process. The three different weld categories defined as under-weld, good-weld and over-weld were studied. The welding mechanisms of each weld categories were different from others. The main input parameters i.e. amplitude, pressure and time, had the main impact on the welding mechanism. The classification of the weld categories is described in section 3.3.

In under-weld, the input energy on the weld was less than the other two categories. Hence, the materials were not deformed much and the material flow was not sufficient to have a good intermixing. That was prominent at the Al-Al interface 2 and Al-Cu interface (Fig. 5). The gap at these interfaces was the main reason for low weld strength. Furthermore, the insufficient material flow was noticed when the materials were not fused properly at the crests (Fig. 5c); although, there was some evidence of material micro-bonds formation and material clinching at the Al-Cu interface (Fig. 5f). This material micro-bonds and clinching were not continuous throughout the interface (Fig. 5g), rather it was intermittent for under-weld when insufficient weld energy was put to the weldments. However, the material mixing was proper at the Al-Al interface 1 (Fig. 5e). This happened because the sonotrode peaks were impinged on the top surface of Al_{top} layer and a sufficiently high amount of weld energy was confined at the Al-Al interface 1. Overall, the material deformation was quite less due to less weld energy and the post-weld thickness was appeared to be within 85% - 100% of the undeformed material thickness before welding (Fig. 4). The low strength at the Al-Cu interface was further justified from the flat fracture surface with comparatively less material sticking (Fig. 14).

In good-weld, the applied weld energy was higher than that of under-weld and subsequently, the material deformation was higher. The post-weld thickness was in the range of 40% to 70% of the unwelded specimen (Fig. 4). The material flow and material intermixing were sufficient enough such that the weld strength obtained from the lap shear and T-peel tests were higher and the fracture surface contained dimple fracture (Fig. 15). This confirmed the material micro-bonds formation and material clinching throughout the Al-Cu weld interface. The optical micrograph (Fig. 6) shows that the micro-bond formation and material clinching at the Al-Al interface 1, Al-Al interface 2 and Al-Cu interface. There was no gap in the material mixing in the good-weld except at some crests. The material was not fused properly at the crest and a slight gap was observed at the crest (Fig. 6b). However, the material mixing at the crest did not contribute much during the lap shear and T-peel tests. Therefore, slight higher weld energy may be put on the weldments in order to fill this gap.

In over-weld, the weld energy applied to the metal was highest of all the weld categories. This produced the highest material deformation and the post-weld thickness was less than 30% of the parent metal thickness (Fig. 4). In this weld category, the material intermixing was so intense that no prominent weld line was appeared in between two conjugative Al layers (Fig. 7). In addition, the micro-bond formation and material clinching at the Al-Cu interface were severe (Fig. 7d and Fig. 7f). As a result, it was difficult to separate the Al layers from Cu layer and the fracture shows the circumferential fracture (nugget pullout) (Fig. 16). The excessive material flow made the joint weaker around the circumference of the weld and hence, the fracture happened at the circumference of the weld during the lap shear and T-peel tests. The material fusion at the crest was intense and there was no gap or unbonded region at the crest in the over-weld (Fig. 7b).

4.3 Layer wise micro-hardness analysis

Layer wise micro-hardness values for all weld categories are presented in section 3.4. At the starting of the welding process, the sonotrode tips impinged on the top surface of Al_{top} layer. All the weld energy was imposed on the top layer and hence deformation at this layer was enormous. Due to the plastic deformation, the material flow was observed towards the valley of sonotrode and the crest was formed (Fig. 12d). The evidence of severe plastic deformation is shown at forged zone in Fig. 12e. The deformation was then extended towards the interface of Al-Cu and finally, the welding occurred at this interface. Thus, Al_{middle} layer had a higher micro-hardness than the Al_{top} layer (micro-hardness measured at crest locations) and Al_{bottom} layer for under-weld (Fig. 9 and Fig. 10). However, due to heat generation and thermal softening [6] for good-weld and over-weld, the micro-hardness values at the three Al layers were remained below than the as-received micro-hardness of Al sheet (Fig. 9 and Fig. 10). The thermal softening further resulted in dynamic recrystallization and the as-received cold worked grains were converted to nearly equiaxed grains (Fig. 13h-i) for good-weld and over-weld.

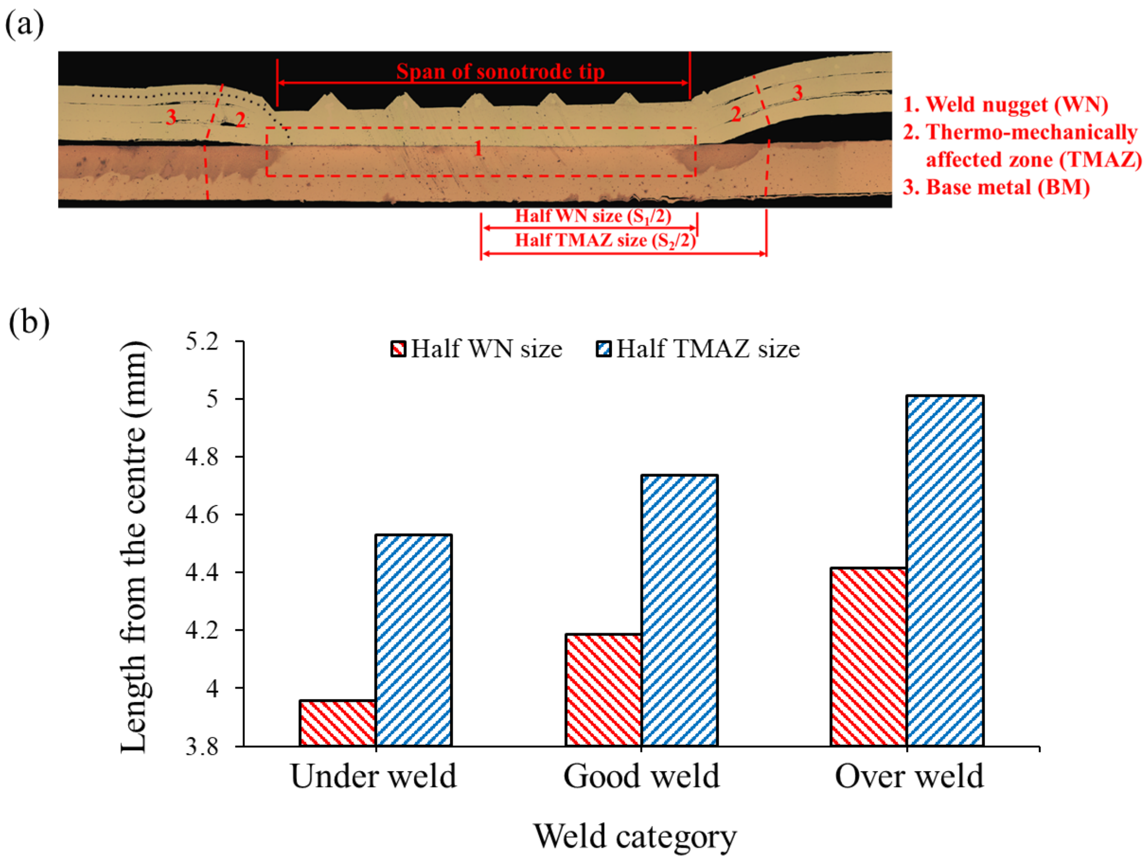

Fig. 17: (a) Classification of weld regions indicating the dimension of each region and (b) variation of half WN size and half TMAZ size with weld category.

The entire area in a welded sample can be divided into three distinct zones [7, 18] mentioned in Fig. 17a. The actual interfacial bonding occurred at area '1', which is called weld nugget (WN). During USW, the severe plastic deformation induced micro-bonding and temperature rise at the metal-to-metal contact areas and the temperature rise aided to recrystallize the grain structure. Area '2' was affected by both plastic deformation and temperature rise; and it was named as thermo-mechanically affected zone (TMAZ). Area '3' was not affected by deformation and temperature rise, and it remained the same in term of microstructure and material properties as base metal (BM). These areas are superimposed on the optical micrograph of the weld cross-section of good-weld and presented in Fig. 17a.

Strength of the weld is generally based on the failure mechanism during destructive tests [21]. In tensile lap shear test, the failure mechanism was different for all the three weld categories as discussed in section 3.6. This difference could be attributed to the changes in microstructure and mechanical properties with space and time [6], [17]. Thus, the location of stress concentration was varied during the lap shear test and the failure location was different for three different weld categories. Hence, a qualitative relationship between the weld category and the size variation of the weld region (i.e., WN, TMAZ) within each weld categories needed to be established. The boundaries between each weld zone (e.g. WN to TMAZ or TMAZ to BM) were evaluated by the locations where the micro-hardness curve changed its gradient [7, 18] as shown in Fig. 11b. For instance, the micro-hardness curve of good-weld exhibited a sudden increase at a location away from the outermost sonotrode teeth (~1.5mm). The micro-hardness profile went past its highest point and then reduced to the micro-hardness of as-received material at the location quite far from the outermost sonotrode teeth (~2.7mm). The first transition region was considered as the boundary of the WN to TMAZ while the latter one was regarded as the boundary of the TMAZ to BM. Half sizes of WN and TMAZ regions (represented in Fig. 17a) of these three weld categories were estimated from the micro-hardness profiles for the respective weld categories and are presented in Fig. 17b. It is evident from Fig. 17b that half TMAZ size increased more sharply than half WN size when the weld categories were shifting from under-weld to over-weld surpassing the good-weld. The half WN size was related to the actual bonding zone during USW [6], [17] and it was increased with the increase of weld energy when welding was shifting from under-weld to over-weld surpassing good-weld. On the other hand, TMAZ was the total affected zone of plastic deformation and temperature rise [6], [17]. The TMAZ zone was increased at a much higher rate than the weld energy input. Hence, the half TMAZ size was increased more rapidly when welding was shifting from under-weld to over-weld surpassing good-weld.

4.4 Grain formation study

In USW, the compressive force was applied on the weldments, which was caused by the opposing teeth of the sonotrode tips and resulted in a net average compressive strain through the sheet thickness [21]. In addition, a net shear strain was also imposed on the weld sheets, as there was a tendency for the sonotrode tips to be displaced, relative to each other while the welding process was going on. The sonotrode was designed to vibrate under the applied compressive clamping pressure and due to the coupled effects of vibration and pressure, they deflected the weld material laterally as the material softens and the entire weld zone started to plastically deform [21].

During USW, generated shear and compressive strains by the ultrasonic vibration caused the plastic deformation primarily in the aluminium weldment sheets of Al-Cu joints leading to the formation of a fine grain structure at the weld interface. This plastic deformation accompanied by vibration resulted in heat generation at the interface as well as at the entire weld zone. The heat softened the materials and caused grain structure evolution. In under-weld, a large volume of low angle grain boundaries was formed and subsequently, they rotate to become high angle, which resulted in the formation of a thin layer of fine grain structure at the interface (Fig. 13g). This phenomenon is widely called as a continuous dynamic recrystallization mechanism during USW process [18], [31]. For good-weld and over-weld, heat generation was increased to a higher level and the average grain size of aluminium at the interface became larger while the overall density of low angle boundaries was reduced (Fig. 13h-i). This could be attributed to boundary migration of the recrystallized grains occurring at higher temperatures [18]. Furthermore, the lower density of low angle boundaries could be related to dislocation annihilation due to dynamic recovery at higher temperature [18]. As soon as the dislocations were formed, they disappeared at a higher temperature during the USW process. Local migration of high angle grain boundaries might also lead to low angle grain boundary annihilation at higher temperature [18], [31]. Overall, the entire Al weld zone was a recovered deformation structure, with a thin band of Al grains near the weld interface showing evidence of severe deformation leading to the formation of fine grains. Far from the weld interface, the distorted parent grain structure can be observed for under-weld while it was absent in good-weld and over-weld due to dynamic recrystallization of the grains. On the other hand, the grains at the top surface follows the flow pattern that was consistent with the deformation induced by the impression of the sonotrode tips.

In order to visualise the texture formation in the recrystallized regions of good-weld and over-weld, the EBSD mapping was performed and shown in Fig. 18 with indicating the inverse pole figure (IPF) Z colour coding. It was prominent that the grains oriented in [101] Z direction in the recrystallized region were low in good-weld while it increased in over-weld. The amount of recrystallized grains was more in over-weld than good-weld and it seemed that during crystallization more grains were oriented in [101] Z direction in over-weld. Hence, at the recrystallized region, the texture formation along [101] Z direction was less in good-weld while the over-weld showed strong texture along [101] Z direction.

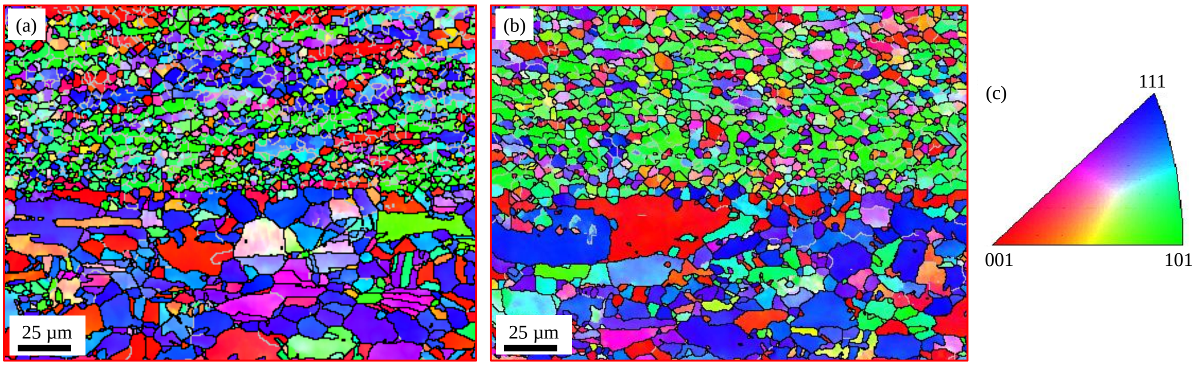

Fig. 18: EBSD mapping of the grains (a) good-weld and (b) over-weld with (c) inverse pole figure (IPF) Z colouring.

Grain boundary fraction of low angle (LAGB) and high angle (HAGB) grain boundaries [39] in all the weld categories (i.e. under-weld, good-weld and over-weld) were calculated from the EBSD map of Al-Cu interfaces (Fig. 13g-i) of respective weld categories and presented in Fig. 19. Good-weld shows the highest HAGB fraction followed by over-weld and under-weld while the LAGB fraction follows exactly the opposite trend of that of HAGB for different weld categories. Actually, HAGB hindered the dislocation gliding and increased the dislocation density at the grain boundary. The accumulated dislocations cancelled the dislocation movement emerging from the applied stress field and consequently the strain energy accumulated at the grain boundary [40]. The plastic deformation occurred when the accumulated strain energy reached a threshold value. As good-weld posed higher HAGB fraction than other two weld categories, the number of accumulated dislocations was higher in the good-weld. Hence, the good-weld provided relatively higher weld strength than the other two weld categories because of the higher amount of stress to be applied for plastic deformation to occur and proceeded to weld failure during lap shear test.

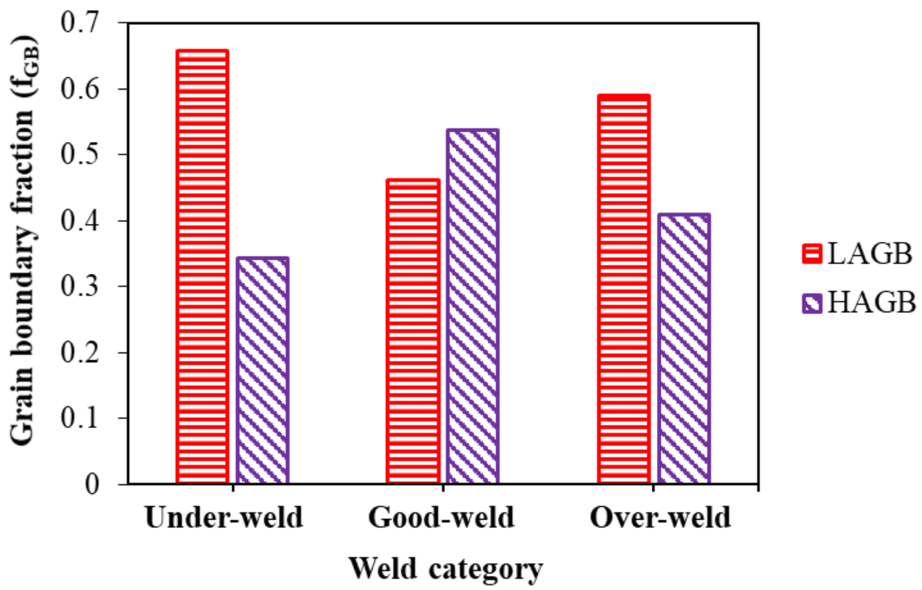

Fig. 19: Grain boundary fraction of low angle (LAGB) and high angle (HAGB) grain boundaries in different weld categories i.e. under-weld, good-weld and over-weld

5 Conclusions

In-depth joint behaviours of multi-layered Al-Cu dissimilar joints (i.e. three layers of 0.3 mm Al tabs ultrasonically welded to 1.0 mm single Cu busbar) to represent electric vehicle battery interconnects were investigated in this paper. The effects of input process parameters (i.e. the amplitude of vibration, welding pressure and welding time) on joint strength, formation of weld microstructure, micro-hardness distribution, layer-wise grain distribution at Al layers and fracture surfaces from tensile tests were analysed for the understanding of multi-layered Al-Cu ultrasonic joints. In-depth analysis was conducted on ultrasonic weld specimens based on the three identified weld categories: under-weld, good-weld and over-weld. Based on the results obtained from this study, the following conclusions were drawn:

- Lap shear and T-peel strengths were used to classify the three weld categories, i.e. under-weld, good-weld and over-weld. These weld categories were further associated with typical weld energy ranges. In case of lap shear, under-weld and over-weld were produced under 400 J and over 700 J respectively, and good-weld was produced in-between under- and over-welds. These values for the T-peel tests were around 650 J and 740 J respectively.
- Study of weld microstructure and material flow revealed the layer-wise bond formation including a wavy interface layer showing mixing of materials, clinching of materials, and wave-like interface of micro-bonds.

- Work hardening and thermal softening were observed at the weld nugget as an effect of process parameters. In case of under-weld, micro-hardness was increased by 8% in comparison with as-received material due to cold work or work hardening. In contrast, micro-hardness values for good-weld and over-weld were measured around 23% and 28% below than the as-received material due to temperature rise and subsequent thermal softening during the welding.
- Crystallographic orientation and grain distribution by EBSD maps of good-weld revealed the material flow, severely deformed fine grains (~5µm) at the Al-Cu interface), a highly deformed forged zone beneath the Sonotrode tips, and an intermediate region with relatively coarse elongated grains (~13µm).
- Higher grain boundary fraction of high angle boundary was the reason for higher weld strength in good-weld. In over-weld, the lower density of high angle boundaries was related to dislocation annihilation due to dynamic recovery at a higher temperature in comparison with good-weld.
- The fracture analysis using SEM revealed the weld interface failure for under-weld, partial nugget fracture with a material tear for good weld and circumferential failure for over-weld. The insufficient bonding was observed for under-weld whereas a characteristic dimple-rupture and a ductile fracture around the weld nugget were the main failure modes for good-weld and over-weld, respectively.

Acknowledgements

This research is partially supported by Research and Development Fund (RDF) from the University of Warwick and WMG Centre High Value Manufacturing (HVM) Catapult for characterisation and testing.

References

[1] R. Faria, P. Moura, J. Delgado, and A. T. de Almeida, “A sustainability assessment of electric vehicles as a personal mobility system,” *Energy Convers. Manag.*, vol. 61, pp. 19–30, 2012.

[2] A. Das, D. Li, D. Williams, and D. Greenwood, “Joining technologies for automotive battery systems manufacturing,” *World Electr. Veh. J.*, vol. 9, no. 2, p. 22, 2018.

[3] X. Wu, T. Liu, and W. Cai, “Microstructure, welding mechanism, and failure of Al/Cu ultrasonic welds,” *J. Manuf. Process.*, vol. 20, pp. 321–331, 2015.

[4] A. Das, A. Barai, I. Masters, and D. Williams, “Comparison of tab-to-busbar ultrasonic joints for electric vehicle Li-ion battery applications,” *World Electr. Veh. J.*, vol. 10, no. 3, p. 55, 2019.

[5] A. Das, T. R. Ashwin, and A. Barai, “Modelling and characterisation of ultrasonic joints for Li-ion batteries to evaluate the impact on electrical resistance and temperature raise,” *J. Energy Storage*, vol. 22, pp. 239–248, 2019.

[6] S. Shawn Lee, T. Hyung Kim, S. Jack Hu, W. W. Cai, J. A. Abell, and J. Li, “Characterization of Joint Quality in Ultrasonic Welding of Battery Tabs,” *J. Manuf. Sci. Eng.*, vol. 135, no. 2, Mar. 2013.

[7] A. Das, D. Li, D. Williams, and D. Greenwood, “Weldability and shear strength feasibility study for automotive electric vehicle battery tab interconnects,” *J. Brazilian Soc. Mech. Sci. Eng.*, vol. 41, no. 1, p. 54, 2019.

[8] U. F. Shaikh, A. Das, A. Barai, and I. Masters, “Electro-Thermo-Mechanical Behaviours of Laser Joints for Electric Vehicle Battery Interconnects,” in *2019 Electric Vehicles International Conference (EV)*, 2019, pp. 1–6.

[9] F. Haddadi, “Microstructure reaction control of dissimilar automotive aluminium to galvanized steel sheets ultrasonic spot welding,” *Mater. Sci. Eng. A*, vol. 678, pp. 72–84, 2016.

[10] C. Q. Zhang, J. D. Robson, and P. B. Prangnell, “Dissimilar ultrasonic spot welding of aerospace aluminum alloy AA2139 to titanium alloy TiAl6V4,” *J. Mater. Process. Technol.*, vol. 231, pp. 382–388, 2016.

[11] Y. Y. Zhao, D. Li, and Y. S. Zhang, “Effect of welding energy on interface zone of Al–Cu ultrasonic welded joint,” *Sci. Technol. Weld. Join.*, vol. 18, no. 4, pp. 354–360, May 2013.

[12] A. Macwan and D. L. Chen, “Microstructure and mechanical properties of ultrasonic spot welded copper-to-magnesium alloy joints,” *Mater. Des.*, vol. 84, pp. 261–269, 2015.

[13] Y. C. Chen and K. Nakata, “Effect of tool geometry on microstructure and mechanical properties of friction stir lap welded magnesium alloy and steel,” *Mater. Des.*, vol. 30, no. 9, pp. 3913–3919, 2009.

[14] U. Dressler, G. Biallas, and U. Alfaro Mercado, “Friction stir welding of titanium alloy TiAl6V4 to aluminium alloy AA2024-T3,” *Mater. Sci. Eng. A*, vol. 526, no. 1, pp. 113–117, 2009.

[15] A. H. Plaine, A. R. Gonzalez, U. F. H. Suhuddin, J. F. dos Santos, and N. G. Alcântara, “The optimization of friction spot welding process parameters in AA6181-T4 and Ti6Al4V dissimilar joints,” *Mater. Des.*, vol. 83, pp. 36–41, 2015.

[16] M. P. Satpathy and S. K. Sahoo, “Mechanical performance and metallurgical characterization of ultrasonically welded dissimilar joints,” *J. Manuf. Process.*, vol. 25, pp. 443–451, 2017.

[17] M. Shakil, N. H. Tariq, M. Ahmad, M. A. Choudhary, J. I. Akhter, and S. S. Babu, “Effect of ultrasonic welding parameters on microstructure and mechanical properties of dissimilar joints,” *Mater. Des.*, vol. 55, pp. 263–273, 2014.

[18] F. Haddadi and F. Abu-Farha, “The effect of interface reaction on vibration evolution and performance of aluminium to steel high power ultrasonic spot joints,” *Mater. Des.*, vol. 89, pp.

50–57, 2016.

[19] P. Prangnell, F. Haddadi, and Y. C. Chen, “Ultrasonic spot welding of aluminium to steel for automotive applications—microstructure and optimisation,” *Mater. Sci. Technol.*, vol. 27, no. 3, pp. 617–624, Mar. 2011.

[20] M. Annoni and M. Carboni, “Ultrasonic metal welding of AA 6022-T4 lap joints: Part I – Technological characterisation and static mechanical behaviour,” *Sci. Technol. Weld. Join.*, vol. 16, no. 2, pp. 107–115, Feb. 2011.

[21] D. Bakavos and P. B. Prangnell, “Mechanisms of joint and microstructure formation in high power ultrasonic spot welding 6111 aluminium automotive sheet,” *Mater. Sci. Eng. A*, vol. 527, no. 23, pp. 6320–6334, 2010.

[22] A. Macwan and D. L. Chen, “Ultrasonic spot welding of rare-earth containing ZEK100 magnesium alloy to 5754 aluminum alloy,” *Mater. Sci. Eng. A*, vol. 666, pp. 139–148, 2016.

[23] A. Panteli, J. D. Robson, I. Brough, and P. B. Prangnell, “The effect of high strain rate deformation on intermetallic reaction during ultrasonic welding aluminium to magnesium,” *Mater. Sci. Eng. A*, vol. 556, pp. 31–42, 2012.

[24] H. T. Gencsoy, J. A. Adams, and S. Shin, “On some fundamental problems in ultrasonic welding of dissimilar metals: Gencsoy, HT, Adams, JA and Shin S. Welding journal, 46, no. 4, p. 145-s (1967),” *Ultrasonics*, vol. 5, no. 4, p. 274, 1967.

[25] S. Matsuoka, “Ultrasonic welding of ceramic/metal,” *J. Mater. Process. Technol.*, vol. 47, no. 1, pp. 185–196, 1994.

[26] S. Matsuoka and H. Imai, “Direct welding of different metals used ultrasonic vibration,” *J. Mater. Process. Technol.*, vol. 209, no. 2, pp. 954–960, 2009.

[27] Y.-C. Chen, D. Bakavos, A. Gholinia, and P. B. Prangnell, “HAZ development and accelerated post-weld natural ageing in ultrasonic spot welding aluminium 6111-T4 automotive sheet,” *Acta Mater.*, vol. 60, no. 6, pp. 2816–2828, 2012.

[28] C. Y. Kong, R. C. Soar, and P. M. Dickens, “Characterisation of aluminium alloy 6061 for the ultrasonic consolidation process,” *Mater. Sci. Eng. A*, vol. 363, no. 1, pp. 99–106, 2003.

[29] S. J. Hu, J. Senkara, and H. Zhang, “Performance characteristics of resistance spot welds in the automotive industry: A structural point of view,” in *Proceedings of IBEC*, 1996, vol. 96, pp. 91–98.

[30] E. T. Hetrick *et al.*, “Ultrasonic Metal Welding Process Robustness in Aluminum Automotive Body Construction Applications,” *Weld. J.*, vol. 88, p. 149–s, Jul. 2009.

[31] A. Macwan, V. K. Patel, X. Q. Jiang, C. Li, S. D. Bhole, and D. L. Chen, “Ultrasonic spot welding of Al/Mg/Al tri-layered clad sheets,” *Mater. Des.*, vol. 62, pp. 344–351, 2014.

[32] R. Balasundaram, V. K. Patel, S. D. Bhole, and D. L. Chen, “Effect of zinc interlayer on ultrasonic spot welded aluminum-to-copper joints,” *Mater. Sci. Eng. A*, vol. 607, pp. 277–286, 2014.

[33] A. Das, I. Masters, and D. Williams, “Process robustness and strength analysis of multi-layered dissimilar joints using ultrasonic metal welding,” *Int. J. Adv. Manuf. Technol.*, vol. 101, no. 1, pp. 881–900, 2019.

[34] F. A. Mirza, A. Macwan, S. D. Bhole, D. L. Chen, and X.-G. Chen, “Effect of welding energy on microstructure and strength of ultrasonic spot welded dissimilar joints of aluminum to steel sheets,” *Mater. Sci. Eng. A*, vol. 668, pp. 73–85, 2016.

[35] F. A. Mirza, A. Macwan, S. D. Bhole, D. L. Chen, and X.-G. Chen, “Microstructure, tensile and fatigue properties of ultrasonic spot welded aluminum to galvanized high-strength-low-alloy and low-carbon steel sheets,” *Mater. Sci. Eng. A*, vol. 690, pp. 323–336, 2017.

[36] V. K. Patel, S. D. Bhole, and D. L. Chen, “Ultrasonic spot welded AZ31 magnesium alloy: Microstructure, texture, and lap shear strength,” *Mater. Sci. Eng. A*, vol. 569, pp. 78–85, 2013.

[37] Z. L. Ni and F. X. Ye, “Dissimilar Joining of Aluminum to Copper Using Ultrasonic Welding,” *Mater. Manuf. Process.*, vol. 31, no. 16, pp. 2091–2100, Dec. 2016.

[38] T. H. Kim, J. Yum, S. J. Hu, J. P. Spicer, and J. A. Abell, “Process robustness of single lap ultrasonic welding of thin, dissimilar materials,” *CIRP Ann.*, vol. 60, no. 1, pp. 17–20, 2011.

[39] S. M. A. K. Mohammed, S. S. Dash, X. Q. Jiang, D. Y. Li, and D. L. Chen, “Ultrasonic spot welding of 5182 aluminum alloy: Evolution of microstructure and mechanical properties,” *Mater. Sci. Eng. A*, vol. 756, pp. 417–429, 2019.

[40] A. Ma, F. Roters, and D. Raabe, “On the consideration of interactions between dislocations and grain boundaries in crystal plasticity finite element modeling – Theory, experiments, and simulations,” *Acta Mater.*, vol. 54, no. 8, pp. 2181–2194, 2006.